NOVA SCHOOL OF SCIENCE & TECHNOLOGY

DEPARTAMENT OF MATERIALS SCIENCE

JOÃO MARIA PIRES SALGUEIRO

BSc in Materials Science and Engineering

3D PRINTED TiO_2 NANOSTRUCTURES FOR WATER PURIFICATION USING SUNLIGHT

INTEGRATED MASTERS IN MATERIALS SCIENCE AND ENGINEERING

NOVA University Lisbon

November, 2023

NOVA SCHOOL OF SCIENCE & TECHNOLOGY

DEPARTAMENT OF MATERIALS SCIENCE

3D PRINTED TIO_2 NANOSTRUCTURES FOR WATER PURIFICATION USING SUNLIGHT

JOÃO MARIA PIRES SALGUEIRO

BSc in Materials Science and Engineering

Adviser: Daniela da Silva Nunes Gomes
Assistant Professor, NOVA University Lisbon

Co-advisers: Ana Cláudia Madeira Botas Gomes Pimentel
Associate Researcher, NOVA University Lisbon

Examination Committee:

Chair:

Rapporteurs:

Adviser:

Members:

MASTER IN MATERIALS SCIENCE AND ENGINEERING

NOVA University Lisbon
November, 2023

3D printed TiO_2 nanostructures for water purification using sunlight

Faber est quisque fortunae saue.

ACKNOWLEDGMENTS

Em primeiro lugar, gostaria de expressar toda a minha sincera gratidão às pessoas e instituições que desempenharam um papel crucial na conclusão desta tese. O vosso apoio, orientação e incentivo foram inestimáveis ao longo desta jornada académica.

Estendo a minha mais profunda gratidão às minhas orientadoras de tese, Prof.ª Daniela Gomes e Prof.ª Ana Pimentel pelo apoio inabalável, feedback perspicaz e orientação dedicada. O conhecimento, a experiência e o estímulo que me foram passados através de horas intermináveis no laboratório, foram fundamentais para moldar a direção da minha pesquisa.

Também sou grato aos membros do corpo docente do Departamento de Ciências de Materiais (DCM) pela sua sabedoria académica e pelo ambiente de aprendizagem enriquecedor que proporcionaram.

Um agradecimento sincero ao CENIMAT e CEMOP, onde conduzi uma grande parte da minha pesquisa. As instalações de última geração (apesar de terem as suas falhas e avarias) e a atmosfera colaborativa foram essenciais para aprimorar a qualidade do meu trabalho.

Reconheço o apoio recebido do DCM e da School of Science and Technologies da Universidade NOVA de Lisboa. O incentivo e os recursos fornecidos foram cruciais para a conclusão bem-sucedida desta tese.

Aos meus amigos e familiares, devo uma dívida de gratidão pelo apoio inabalável e compreensão. O estímulo que me proporcionaram gerou a força emocional necessária para enfrentar os desafios da academia. Um agradecimento mais que eterno e especial à Leonor Matias e à Ana Metelo. Leonor, foste mais que uma colega, foste uma mentora dentro e fora do laboratório. Contigo aprendi tudo aquilo que sei sobre o que é a vida de um investigador. Por tudo aquilo que fizeste, mil obrigados. Ana, contigo partilhei esta jornada desconhecida e assustadora que é escrever uma tese. Sem dúvida alguma que todo este processo foi muito melhor ao saber que estávamos os dois no mesmo barco. Por tudo o que fizeste por mim, muito obrigado.

Quero expressar minha mais profunda gratidão à minha família, que agora já sabem o que um "quase" engenheiro faz. Por todos os sacrifícios, incentivos e crenças nas minhas habilidades. O vosso apoio inabalável tem sido minha âncora ao longo desta empreitada académica.

ABSTRACT

In this dissertation, it is explored the application of 3D printing to create structures containing titanium dioxide (TiO_2) nanoparticles for water purification using sunlight. The nanoparticles used were efficiently synthesized at low temperatures through a microwave-assisted solvothermal method, in comparison to conventional methods. The stereolithographic printing technique was employed to produce mesoporous structures with various dimensions and cavities. Two methods were used to introduce nanoparticles into the mesoporous structures: the microwave method (*in-situ*) and the dip-coating technique. Different solvents and catalysts were used for subsequent structural, morphological, and photocatalytic efficiency analyses. Photocatalysis tests conducted using a sunlight simulator revealed that the TiO_2 sample synthesized at higher temperature and pressure, using ethanol as a solvent during synthesis, exhibited the best performance, degrading approximately 85% of RhB in 120 minutes. Subsequently, tests of photocatalysis under natural sunlight and reuse tests were conducted on the most effective sample.

Structural and morphological characterizations of the nanoparticles were performed using scanning electron microscopy (SEM), X-ray diffraction (XRD), Raman spectroscopy and scanning transmission electron microscopy (STEM). Additionally, optical measurements were also carried out to access the optical band gap values of the powder materials.

This approach represents an effective alternative to produce macroporous materials with TiO_2, as 3D printing stands out as an economical, simple, fast, and versatile technique in part production, enabling its application in various industrial contexts.

Keywords: 3D printing, TiO_2 nanoparticles, photocatalysis, RhB, sunlight, dip coating, microwave irradiation.

RESUMO

Nesta dissertação, explora-se a aplicação da impressão 3D para criar estruturas contendo nanopartículas de dióxido de titânio (TiO_2) para a purificação da água por meio da luz solar. As nanopartículas utilizadas foram sintetizadas de maneira eficiente e a baixa temperatura por meio de um método solvotermal assistido por radiação de micro-ondas, em comparação com os métodos convencionais. Utiliza-se a técnica de impressão estereolitográfica para produzir estruturas mesoporosas com diversas dimensões e cavidades. Dois métodos foram empregues para introduzir as nanopartículas nas estruturas, como o método de micro-ondas (*in-situ*) e técnica de dip coating. Utilizaram-se diferentes tipos de solventes e de catalisadores para posterior análise estrutural, morfológica e eficácia na fotocatálise. Os testes de fotocatálise realizados através de um simulador de luz solar, revelaram que a amostra de TiO_2 sintetizada a temperatura e pressão mais altas, tendo sido utilizado etanol como solvente durante a síntese da mesma, apresentou a melhor performance, degradando aproximadamente 85% de rodamina B em 120 minutos. Posteriormente, foram conduzidos testes de fotocatálise à luz solar natural e testes de reutilização na amostra mais eficaz.

As caracterizações estruturais e morfológicas das nanopartículas foram realizadas por meio de espectroscopia de raios-X por dispersão de energia (SEM), difração de raios-X (DRX), espectroscopia Raman e microscópio eletrónico de varrimento por transmissão (STEM) . Além disso, a reflectância foi obtida para calcular o hiato energético das nanopartículas.

Esta abordagem representa uma alternativa eficaz para a produção de materiais macroporosos com TiO_2, uma vez que a impressão 3D se destaca como uma técnica económica, simples, rápida e versátil na produção de peças, possibilitando a sua aplicação em contextos industriais variados.

Palavras-chaves: Impressão 3D, nanopartículas de TiO_2, fotocatálise, RhB, luz solar, dip coating, micro-ondas.

CONTENTS

LIST OF FIGURES

LIST OF TABLES

ACRONYMS

AM – Addictive manufacturing

3D -Three dimensional

CB - Conduction band

MW – Microwave

DC – Dip coating

IPA – Isopropyl alcohol

NPs - Nanoparticles

SEM - Scanning electron microscopy

SLA - Stereolithography

RhB – Rhodamine B

UV - Ultraviolet

VB - Valence band

XRD - X-ray diffraction

SYMBOLS

λ - X-ray wavelength

β - Full width at half maximum (FWHM)

θ - Braggs angle

α - Absorption coefficient

ν - Photon’s frequency

D - Crystallite size

K - Dimensionless shape factor

A - Energy independent constant

h - Plank's constant

E_g - Band gap energy

m - Constant exponent

R - Absolute reflectance

k - Absorption coefficient

s - Scattering coefficient

1

INTRODUCTION

1.1 TiO_2 nanostructures

TiO_2 is a widely studied n-type semiconductor with numerous applications, including in sensors [1], dye-solar cells [2], electrochromic devices [3], and as a photocatalyst [4] (which is the most used in the latter application) for purifying water/wastewater and air and in self-cleaning glasses [5]. Anatase, rutile and brookite are the three major crystalline phases of TiO_2, the first one having better photocatalytic activity amongst the three, which can be explained by its indirect band gap.

Anatase possesses an indirect band gap, meaning that the minimum energy in the conduction band (CB) is separated from the greatest energy in the valence band (VB). As a result, excited electrons stabilize at the lowest level of energy in the (CB), slowing down the charge carrier recombination period. The trapping of photogenerated holes on the particle's surface due to the steeper potential band bending also causes spatial charge separation, enhancing the photocatalytic activity [6-10].

Anatase has a wider specific surface area, resulting in more active sites than rutile. The most active facet of anatase is the {001}[11]. Researchers investigated how dissociative adsorption impacts the photoactivity of TiO_2 crystals. They have underscored that a greater proportion of {001} facets is associated with heightened photooxidation reactivity in TiO_2 particles of similar size [12]. These {001} facets are thought to improve the movement of charge carriers, resulting in increased photocatalytic efficiency [13]. The dissociative adsorption on {001} facets lowers activation energy and influences the molecular-level reaction mechanism in photocatalytic processes, showcasing distinctive surface chemistry. Additionally, besides the improved dissociative adsorption, {001} facets assist in the separation of charges generated during photoactivation, thanks to unsaturated Ti atoms and surface defects like oxygen vacancies. This deficiency in oxygen induces specific surface reconstruction, fostering interfacial electron transfer and the separation of charges [14].

Regarding the band gap of all TiO_2 phases, brookite and rutile phases of TiO_2 have band gaps of 3.0 eV, while anatase's phase has a band gap of 3.2 eV, meaning that TiO_2 can be classified as a wide band gap material [3] [15]. This means that higher energy, such as ultra-violet (UV) light, is needed to activate the semiconductor, which can be a limitation for photoactivity under sunlight. However, many studies have proven that working with TiO_2 at the nanoscale with structures such as nanoparticles [16], nanotubes [17] and nanowires [18] makes it possible to absorb light in the visible region. To reduce the band gap energy and improve visible light absorption and minimize charge carrier recombination, it is common to dope TiO_2 with different cations or anions, such as copper (Cu) [19], vanadium (V) [20], iron (Fe) [21], and cobalt (Co) [22].

1.2 Synthesis of nanostructures using microwave-assisted methods

Depending on their intended application, TiO_2 nanoparticles can be synthesized using a variety of methods. Synthesis methods in the liquid phase, such as sol-gel [23], colloidal [24], precipitation [25], and hydrothermal [26], are convenient and have simple synthesis processes with controllable particle size. However, many conventional methods require longer synthesis times, high energy consumption, and can be costly [27].

The use of hydrothermal technology in the synthesis of TiO_2 nanoparticles has been improved over the years, and the addition of microwave (MW) irradiation has been widely successful among the scientific community. During the synthesis process, (MW) heat energy is generated through the conversion of kinetic energy derived from the collision and friction of polar molecules. The (MW) oven magnetron radiates high frequency (MW)s, leading to the (MW) energy field continuously switching polarity at a high speed and frequency. This results in the rearrangement of the molecular motion of polar molecules from disorganized to an ordered high-frequency vibration [28].

The (MW)-assisted synthesis method for TiO_2 nanoparticles has several advantages over conventional methods. It provides faster, saving energy, more uniform heating and a lower synthesis temperature due to the combination of (MW) heating and water heat. It also allows for better control over the crystal size, active facet, and agglomeration through the adjustment of parameters such as the ratio of precursors, reaction pH level, time, and temperature [29-32]. Additionally, this synthesis method allows for the growth of nanostructures on diverse substrates, including glass [33], cork [34], polyester films[35], plastics [36], ceramics [37], microcrystalline cellulose [38] and also 3D printed structures [31], which is the main focus of this work.

1.3 Dip coating

The dip coating (DC) method is a versatile and extensively used approach for applying thin films onto different surfaces, presenting a wide array of uses in various scientific and industrial fields such as in photocatalysis [39-41], optics [42-44], sensors [45-47], electronics [48-50] and biomedical applications [51].

(DC), operates by immersing a substrate into a liquid solution or suspension, ensuring complete coverage by the coating material, and then carefully withdrawing it. Upon withdrawal, the excess solution drains off, leaving a thin film of the coating material adhering to the substrate. Subsequent to the coating step, the substrate is typically left to dry, with the option of additional heat treatment to enhance the film's properties [52], such as adhesion [53] and crystallinity [54].

As every other technique, the (DC) technique has its advantages. One notable advantage is its simplicity and cost-effectiveness [55]. This method requires minimal equipment and resources, making it accessible for various applications. Its versatility is another key strength, as it accommodates different coating materials and substrate types [56]. Additionally, (DC) can achieve uniform coatings on complex shapes and diverse surfaces [57], enhancing its applicability.

However, (DC) does have some limitations. Achieving precise control over film thickness and uniformity can be challenging compared to more sophisticated techniques [58]. The method is primarily suitable for thin films and may have limitations for thicker coatings. Moreover, the properties of the coating solution, such as viscosity and concentration, significantly impact the final film characteristics [59]. Despite these limitations, (DC) remains a valuable and widely used method, particularly when simplicity and cost-effectiveness are prioritized in thin film deposition processes.

1.4 Photocatalysis

Photocatalysis is a chemical phenomenon that involves the use of light and a photoactive material to accelerate a chemical reaction. Typically, it happens as a result of interfacial redox reactions involving electron-hole pairs created at a semiconductor's surface. When the semiconductor is subjected to light with an energy higher than its band gap, photoelectrons in the VB are stimulated to the (CB), leaving holes behind. By causing adsorbed water molecules to oxidize and diffuse to the surface, these holes create hydroxyl radicals (•OH-), which break down both organic and inorganic substances. At the same time, electrons in the (CB) react with molecular oxygen (O_2) in the air, generating superoxide anion radicals (O_2•-) [60-61]. The superoxide ion participates in the oxidation reaction within the TiO_2 molecule and prevents electron-hole recombination.

There are several factors that can limit the photoactivity of TiO_2, including its band gap, the recombination of electron-hole pairs, and a low effective surface area. The dimensional structure of the photocatalytic compound can also influence its performance, as the pore structure, pore volume, and surface area are important consideration [7]. According to Zhang et al . [62], the fabrication of hierarchically porous materials with a large surface area can improve the photocatalytic efficiency of TiO_2. These materials can be used for a number of purposes and can be found in a wide range of architectures, including microparticles, films, core-shell, nanosheets, spheres, nanofibers, and multi-level structures.

1.5 3D printing applied to photocatalysis

The integration of 3D printing with photocatalysis is revolutionizing the field of water purification. Cutting-edge 3D printing techniques, including Digital Light Processing (DLP) [63] and Continuous Liquid Interface Production (CLIP) [64], are facilitating the precise engineering of TiO_2 nanostructures. This engineering breakthrough enables enhanced efficiency in solar-powered water purification, showcasing a pivotal stride toward sustainable technology.

The environmental impact of 3D-printed TiO_2 nanostructures is noteworthy. The inherent eco-friendly nature of this approach minimizes material wastage, offering a compelling green alternative for water treatment. Beyond this, the photocatalytic degradation of contaminants under sunlight adds another layer of eco-friendliness, presenting a promising solution with reduced energy consumption and a diminished ecological footprint [65].

However, challenges persist in the widespread implementation of 3D-printed TiO_2 nanostructures. Scalability, cost-effectiveness, and long-term stability are focal points for ongoing exploration. Researchers are actively delving into novel materials, advanced printing techniques, and the integration of these structures into scalable water treatment systems to address these challenges [66].

In parallel, additive manufacturing (AM) has emerged as a transformative force in photocatalytic studies. AM, known for its simplicity, low cost, and capability to produce complex structures with minimal waste, is making significant contributions [67]. Various 3D printing methods utilizing TiO_2 nanoparticle-based materials, such as powder-based inks [68], show immense potential for water treatment purposes. The incorporation of TiO_2 in filaments for extrusion methods, like fused deposition modeling [69] and robocasting [70], has been extensively studied, highlighting strengths and potential drawbacks.

As technology advances, alternative methods such as SLA 3D printing are gaining prominence [71]. SLA involves curing a liquid photosensitive resin under a UV laser beam, resulting in highly detailed and smooth structures. This technique enhances photocatalysis performance by enabling the creation

of interconnected architectures like scaffolds and honeycombs, offering efficient pollutant diffusion pathways.

This intricate fusion of 3D printing technologies and photocatalysis signifies more than just technological efficiency. It embodies a transformative shift towards sustainable water treatment solutions, combining innovation, precision engineering, and environmental consciousness to address global challenges. Ongoing research and development in this dynamic field promise to unveil even more impactful applications and solutions for the future of water purification [72-76]. Recent studies addressed the use of 3D printed structures in photocatalytic applications with successful breakthroughs in the degradation of air and water pollutants [77-81].

This work aims to develop the next generation of 3D photoactive nanomaterials based on TiO_2 nanostructures. To achieve this, 3D-printing technology will be used to build 3D macro- mesoporous TiO_2 structures that act as active sponges and increase adsorption and photoinduced activation to enhance photocatalysis under sunlight.

2

EXPERIMENTAL PROCEDURE

2.1 Synthesis of TiO2 nanoparticles

Solvothermal method assisted by (MW) irradiation was used to produce and synthesize TiO_2 nanoparticles. Initially, a solution was prepared by adding 2.5 mL of either a 1M solution of anhydrous oxalic acid (Sigma-Aldrich; CAS: 114-62-7) or ammonium hydroxide (Sigma-Aldrich; CAS: 1336-21-6) to 57.5 mL of a chosen solvent (Milipore water, absolute ethanol, or isopropyl alcohol). This solution underwent stirring on a magnetic plate for 5 minutes. To this, 2 mL of titanium (IV) isopropoxide (TTIP) (Sigma-Aldrich; CAS: 546-68-9) was added and stirred until homogenized. The (MW) synthesis was initiated by introducing 20 mL of the final solution into a sealed glass container, which was then placed into the (MW) apparatus (CEM Focused Microwave Synthesis System Discover SP). Two distinct approaches were employed for TiO_2 nanoparticle synthesis, delineated in subsequent tables.

Table 2.1. – Specific parameters of TiO_2 nanoparticles synthesis.

	Approach A	**Approach B**				
	Step 1	Step 1	Step 2	Step 3	Step 4	Step 5
Ramp time (min)	20	20	20	20	20	20
Hold time (min)	60	1	1	1	1	20
Temperature (ºC)	90	100	120	150	170	190
Pressure (PSI)	150	50	100	150	280	280
Power (W)	100	50	100	150	280	280

It is noteworthy to mention that, in total, 9 samples were created based on the two approaches mentioned above. From approach A (in-situ), 6 samples were synthesized corresponding to the number

of combinations of solvents and catalysts (3 solvents and 2 catalysts). From approach B (dip coating), only 3 samples were synthesized. In the table below, all the information about the samples is displayed.

The choice between a basic catalyst, such as ammonium hydroxide and an acid catalyst, like oxalic acid, in the synthesis of TiO_2 nanoparticles introduces nuanced differences with notable implications. Each type of catalyst plays a distinctive role in shaping the properties of the resulting TiO_2 material, with specific advantages and considerations. Their influence extends to the control of particle size, morphology, and crystalline structure, impacting the photocatalytic activity of TiO_2 [82].

Table 2.2 – Information about TiO_2 samples.

Sample's name	Approach	Solvent	Catalyst
A1	A	Milipore water	Anhydrous oxalic acid
A2	A	Absolute ethanol	Anhydrous oxalic acid
A3	A	Isopropyl alcohol	Anhydrous oxalic acid
A4	A	Milipore water	Ammonium hydroxide
A5	A	Absolute ethanol	Ammonium hydroxide
A6	A	Isopropyl alcohol	Ammonium hydroxide
B1	B	Milipore water	Anhydrous oxalic acid
B2	B	Absolute ethanol	Anhydrous oxalic acid
B3	B	Isopropyl alcohol	Anhydrous oxalic acid

Post-(MW) synthesis, the nanoparticles underwent filtration using the Neya 16 Remi Centrifuge. A meticulous washing process ensued, involving three cycles with absolute ethanol, each executed under identical conditions of centrifugation at 5000 rpm for 3 minutes. Subsequently, the cleaned nanoparticles were transferred to a desiccator for drying. This drying process took place at 100 °C under vacuum conditions for a duration of 1 hour. Following drying, the nanoparticles were subjected to grinding and then carefully stored in a receptacle for future utilization. This meticulous procedure ensured the successful synthesis of TiO_2 nanoparticles, incorporating precise catalyst and solvent selections, (MW) irradiation, and thorough post-synthesis processing.

2.2 Designing and printing of the 3D structure

A single structure was conceived using Fusion360, a computer-aided design (CAD) software based in San Francisco, California, USA. To achieve this, the structure was meticulously crafted and materialized using a Form-2 SLA printer, employing liquid resin, specifically Formlabs High Temperature Resin for Heat Resistance.

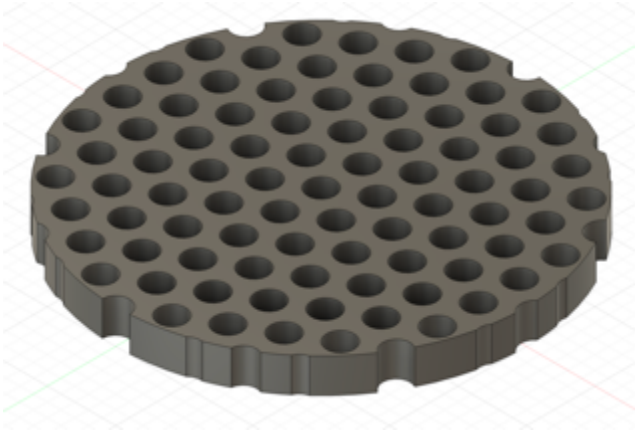

Figure 2.2.1 - Design of the 3D macro mesoporous structure.

This circular structure has 25 mm of diameter and 5 mm of height. In its matrix, each one of the circular holes has a diameter of 1mm, with a depth of 5mm (the structure is seen through), and are separated of each other by 1mm. The 3D structure was taken out of the printer and cleansed using IPA to eliminate any remaining unhardened liquid resin. Subsequently, it was immersed in an IPA bath for 6 minutes [83]. Following this, the untreated specimens were dried and subjected to 30 minutes of ultra-violet (UV) irradiation using the PSD Pro Series Digital UV Ozone System NOVASCAN at a temperature of 60ºC to finalize the polymerization process.

2.3 Impregnation of nanoparticles in the 3D structure

Two different techniques were used for incorporating TiO_2 nanoparticles in the surface of 3D printed structures. The first technique, henceforward known as in-situ (IS), focused on the growth of TiO_2 nanoparticles directly on the 3D structure, by placing it inside the sealed glass container with the solution, during the (MW) irradiation synthesis. The second technique, from now on known as (DC), intended to deposit and coat the 3D structure with already synthesized TiO_2 nanoparticles (via (MW) irradiation synthesis) by submerging it in a stable suspension that contained the TiO_2 nanoparticles.

For the IS method, the parameters used in the synthesis of TiO_2 nanoparticles were the same as in approach A (**Table 2.1**), since the resin of the 3D structure cannot withstand very high temperatures (which would melt in the process).

For the DC method, the parameters used were the same as in approach B (**Table 2.1**). This method allowed for higher synthesis temperatures by not having the 3D structure inside the glass vessel and so, the impregnation of nanoparticles had to be done after the synthesis. To prepare the (DC) solution, two other solutions were made so that a stable suspension was achieved. In the first solution, for each 10 mL of distilled water was added 1 mg of PEG and 1 mg of PAAc and left it to stir for 24 h. In the second solution, for each mL of distilled water was added 2 mg of powder and left it in an ultrasounds

bath for 30 min. Finally, to complete the final (DC) solution, 12 mL of the first solution and 20 mL of the second solution were mixed in a separate container until homogenized. To coat the 3D structure with TiO_2 nanoparticles, a (DC) device was used. The specific parameters of this part were immersion speed, hold time, emergence speed and drying time which were 500 mm/s, 5 s, 500 mm/s and 150 s (for each side), respectfully. To speed up the drying part, a regular hair dryer was used.

To ensure that the 3D structures were coated with the desired amount of 25 mg of nanoparticles, it was weighed before and after each procedure.

2.4 Photocatalysis activity

To test the photocatalytic activity of the 3D printed structures it involved subjecting them to examination using the LED Solar Simulator – LSH-7320 configured at 1 SUN intensity and conducted at room temperature. RhB (RhB) served as the model dye for these experiments. In each trial, the structure was positioned on the recipient platform, and a 50 mL solution of RhB (5mg/L) was agitated for 30 min in darkness to establish adsorption-desorption equilibrium. The absorbance spectra were systematically recorded at 30 min intervals through this period, employing the Spectrometer UV-Vis NIR – Perkin Elmer Lambda 950. To mitigate the issue of solution overheating during the aforementioned tests, the previous recipient was enclosed within a larger receptacle filled with cold water. The rationale behind this procedural modification was rooted in the observed consequence of solution overheating during the experimental trials. This overheating phenomenon induced water evaporation, thereby causing unintended elevation in the concentration of RhB within the solution, thereby distorting the intended outcomes.

For structures exhibiting optimal performance, reusability assessments were undertaken. Furthermore, to substantiate the viability of the proposed methodology, photocatalytic reactions were conducted under natural sunlight conditions, with a cumulative exposure time of 120 min. Solar intensity was quantified using a Sciencetech solar power meter (Sciencetech-Inc, London, ON, Canada) revealing an approximate average value of 0.70 SUN and a UV index of 7 out of 11, as per measurements from the IPMA (Instituto Português do Mar e da Atmosfera) website.

2.5 Characterization techniques

SEM images were captured utilizing the Regulus 8220 Scanning Electron Microscope. The sizing of the nanoparticles was assessed through ImageJ software. For EDS measurements, a Carl Zeiss AURIGA CrossBeam SEM-FIB workstation was employed.

Scanning transmission electron microscopy (STEM) images, including high-angle annular dark-field (HAADF) imaging, were carried out with a Hitachi HF5000 field-emission transmission electron microscope operated at 200 kV (Mito, Japan). This is a cold FEG TEM/STEM with a spherical aberration-corrector for the probe and it is equipped with one 100mm² EDS detectors from Oxford Instruments.

A drop of the sonicated dispersions was deposited onto lacey-carbon copper grids and allowed to dry before observation.

X-ray diffraction (XRD) measurements were conducted using a PANalytical Xpert PRO MFP-3D diffractometer, utilizing CuKα radiation as the X-ray source. The XRD data were collected within a 2θ range of 20º to 90º, with a step size of 0.0334225º, and recorded with an X'Celerator 1D detector. The simulated crystal structures for brookite, rutile, and anatase were referenced to ICDD file No. 01-076-1937, ICSD file No. 96-900-4143, and ICSD file No. 082084, respectively. The simulated anatase structure had lattice parameters (Å) a = b = 3.7830 and c = 9.4970.

Raman spectroscopic measurements were conducted using the inVia Qontor confocal Raman microscope manufactured by Renishaw, located in Kingswood, UK. The excitation source employed was a 50 milliwatt green diode-pumped solid-state laser operating at 532 nanometers. The laser operated with a 10-second exposure time and settings configured for 3 accumulations. Raman spectra were recorded through an extended scan spanning the range of 100 to 700 wave numbers (cm^{-1}). The laser beam was focused using a 50× Olympus objective with a long working distance of 8.2 millimeters. The reported results are derived from the average of multiple scans conducted on the surface of the synthesized powder. To ensure accuracy and account for potential fluctuations in the Raman system, the spectrograph was calibrated using the 521 cm^{-1} peak of a silicon wafer. All measurements were carried out at room temperature.

For optical characterization, the band gap of TiO_2 powders was determined based on reflectance spectra in the 200–800 nm range. This analysis was conducted using a PerkinElmer Lambda 950 UV/VIS/NIR spectrophotometer.

3

RESULTS AND DISCUSSION

Pure TiO_2 nanoparticles with a base and an acid catalyst were synthesized effectively utilizing (MW) irradiation, a method known for its expeditious and low-temperature synthesis characteristics. The subsequent step involved the successful fabrication of a macro-mesoporous structure through the employment of the SLA 3D printing technique. To impart functional attributes, the incorporation of nanoparticles was accomplished through two methodologies: in situ growth and (DC). A comprehensive evaluation was undertaken to gauge the photocatalytic activity of this 3D-printed TiO_2 structure under sunlight simulator conditions. The assessment encompassed an investigation into the impact of structural morphology, the efficacy of both nanoparticle incorporation methods, and the reusability potential of the printed TiO_2 structure. Additionally, the photocatalytic performance of sample B2 was specifically scrutinized under sunlight simulator conditions as part of this comprehensive analysis.

3.1 Morphological and structural characterization of the nanoparticles synthesized under microwave irradiation

3.1.1 XRD measurements

X-ray Diffraction (XRD) analyses were conducted to discern the crystallographic structure of TiO_2-based materials. The powder diffractogram of A1, A2, A3, A4, A5, and A6 TiO_2 nanoparticles is depicted in **Figure 3.1.3**.

The X-ray diffraction patterns (diffractograms) for samples A1, A2, and A3 demonstrate striking similarities, suggesting a common crystalline phase. Upon detailed examination and comparison with simulated diffractograms corresponding to various TiO_2 crystalline phases such as anatase, rutile, and brookite, the experimental patterns notably align with the characteristic peaks of the anatase phase, positioned at 2θ = 25.25º, 37.71º, and 48.01º and assigned, respectively, to (101), (004), and (200) anatase's planes. Furthermore, no additional peaks related to impurities, such as Ti(OH)4, were identified.

However, when examining the diffractograms of A4, A5, and A6, a significant deviation is evident. Not only do these samples fail to correlate with any of the simulated TiO_2 crystalline phases, but they also lack notable peaks altogether. Upon further investigation, we concluded that these samples are likely amorphous, as they do not exhibit similarities with any of the simulated TiO_2 crystalline phases [86].

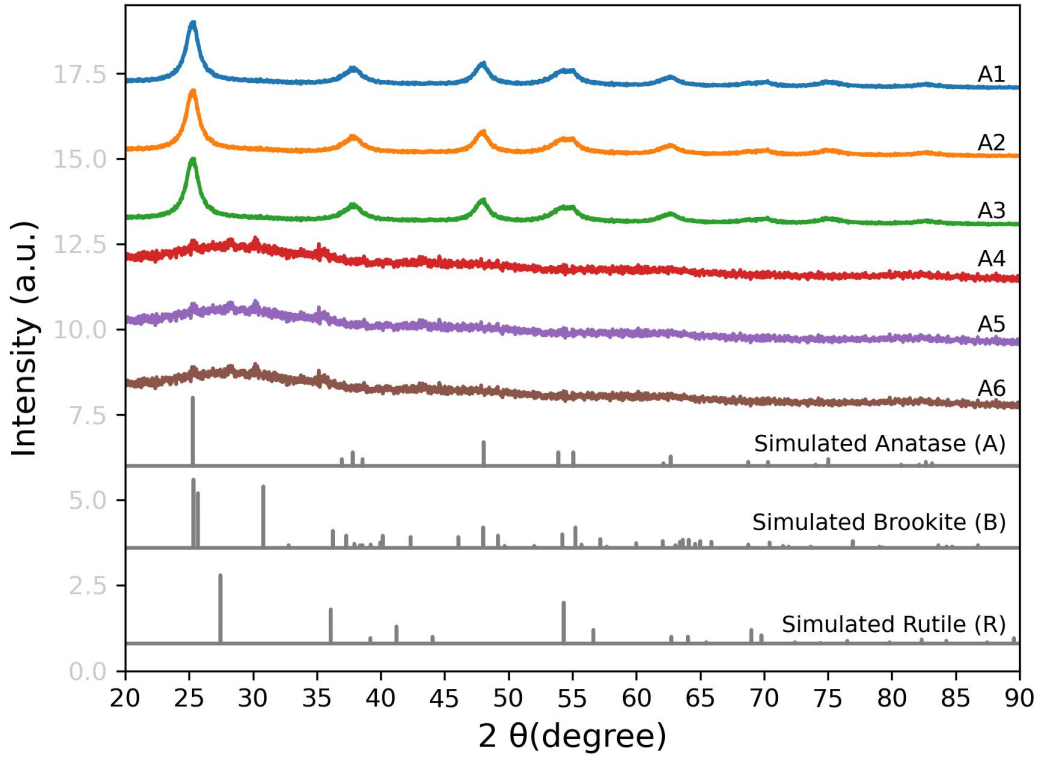

Figure 3.1.1 - XRD diffractograms of A1, A2, A3, A4, A5 and A6. The diffractograms are normalized at the maximum intensity. Simulated rutile, anatase and brookite powder diffractograms are shown for comparison.

As the materials produced with base as precursor resulted in amorphous materials (A4, A5 and A6), they were not considered for further analyses.

3.1.2 SEM analysis

Displayed in **Figure 3.1.1** are presented the SEM images of samples from approach A (**Figure 3.1.1 a**, **b** and **c**) and from approach B (**Figure 3.1.1 d**, **e** and **f**) regarding TiO_2 nanoparticles synthesized under (MW) irradiation. The main difference between SEM images from approach A and B are the size and shape of the nanoparticles. All images display large amounts of nanoparticles in the shape of nanospheres and it can clearly be observed the presence of larger and deformed spheres that resemble nanorods. The average size of the measured nanoparticles from approach A are 9.89 $\pm$ 3.84 nm for A1, 15.32 $\pm$ 3.12 nm for A2 and 7.89 $\pm$ 2.84 nm for A3. From approach B are 17.24 $\pm$ 2.85 nm for B1, 21.32 $\pm$ 4.55 nm for B2 and 15.13 $\pm$ 2.41 nm for B3. With the elevation of pressure and temperature, so do the nanoparticles size gets bigger.

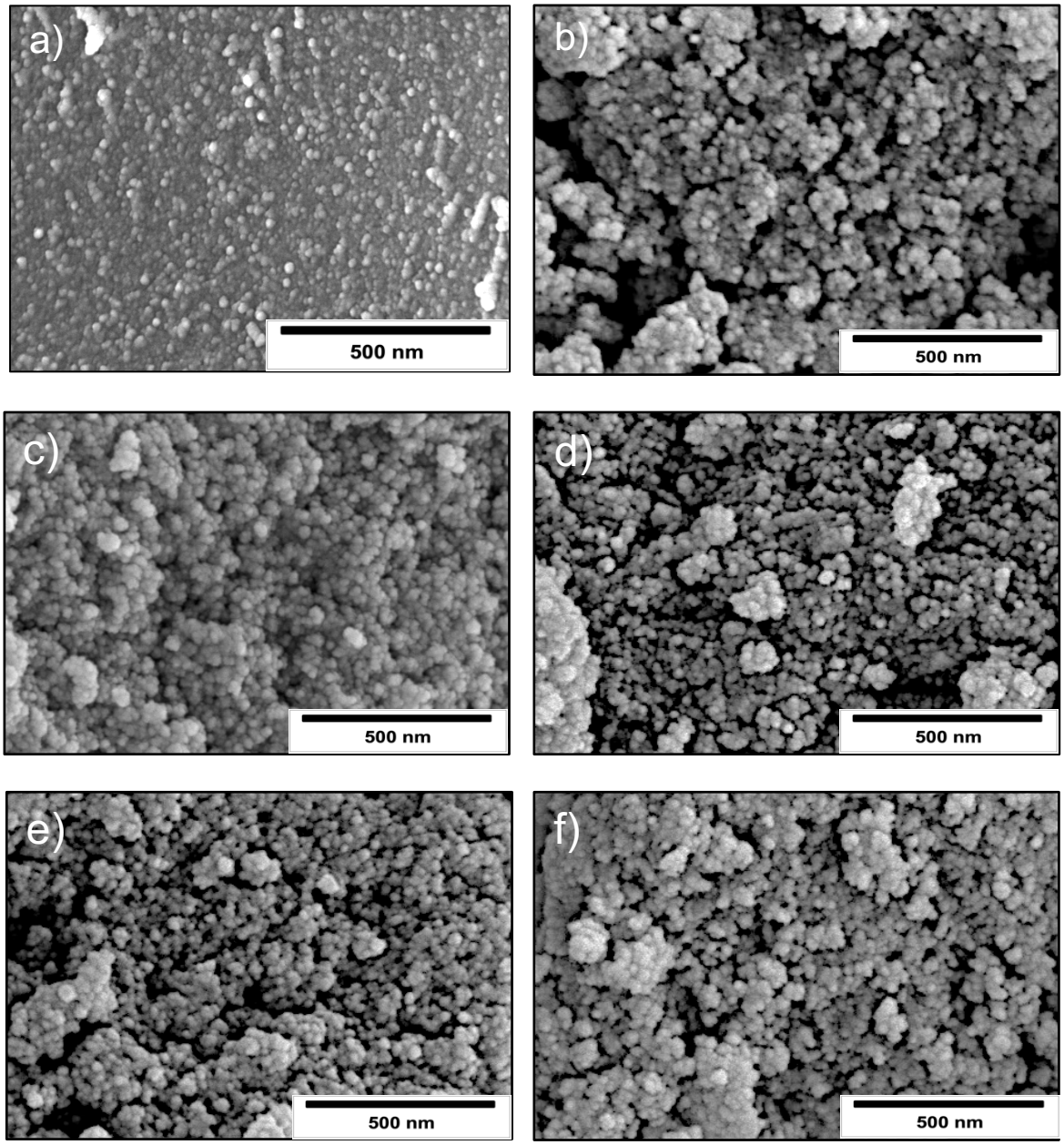

Figure 3.1.2– SEM images of (a) A1, (b) A2, (c) A3, (d) B1, (e) B2 and (f) B3.

3.1.3 STEM analysis

The STEM images of the TiO_2 nanoparticles synthesized using ethanol as solvent and 190 ºC as the temperature of synthesis. It is clear that synthesis resulted in very fine nanoparticles (around 5 nm) that are highly agglomerated (**Figure 3.1.2**. (a) and (b)). From the atomic-resolution HAADF STEM image in **Erro! A origem da referência não foi encontrada.**(c and d), it is clear atomic columns, that from the Z-contrast, it can be assumed the visible spots must correspond to Ti atom [84]. These Ti

atomic columns are perpendicular to each other, and it has been determined to be from the (100) and (010) atomic planes of anatase with a lattice spacing of ≈ 0.378 nm [85]. The insets presented in **Figure 3.1.2**. (d) represent the Fast Fourier Transformation (FFT) images carried out in the TiO_2 nanocrystal magnified in **Figure 3.1.2**. (d). Observed through the [001] zone axis, it is evident from the FFT patterns that the angles (100) and (010) is 90º, in accordance with the theoretical value reported for pure crystalline anatase TiO_2 (ICSD file No. 9852). From the atomic-resolution HAADF images and FFT patterns, it can be inferred the tetragonal atomic arrangement on the (001) surface of the TiO_2 nanocrystals [84-85].

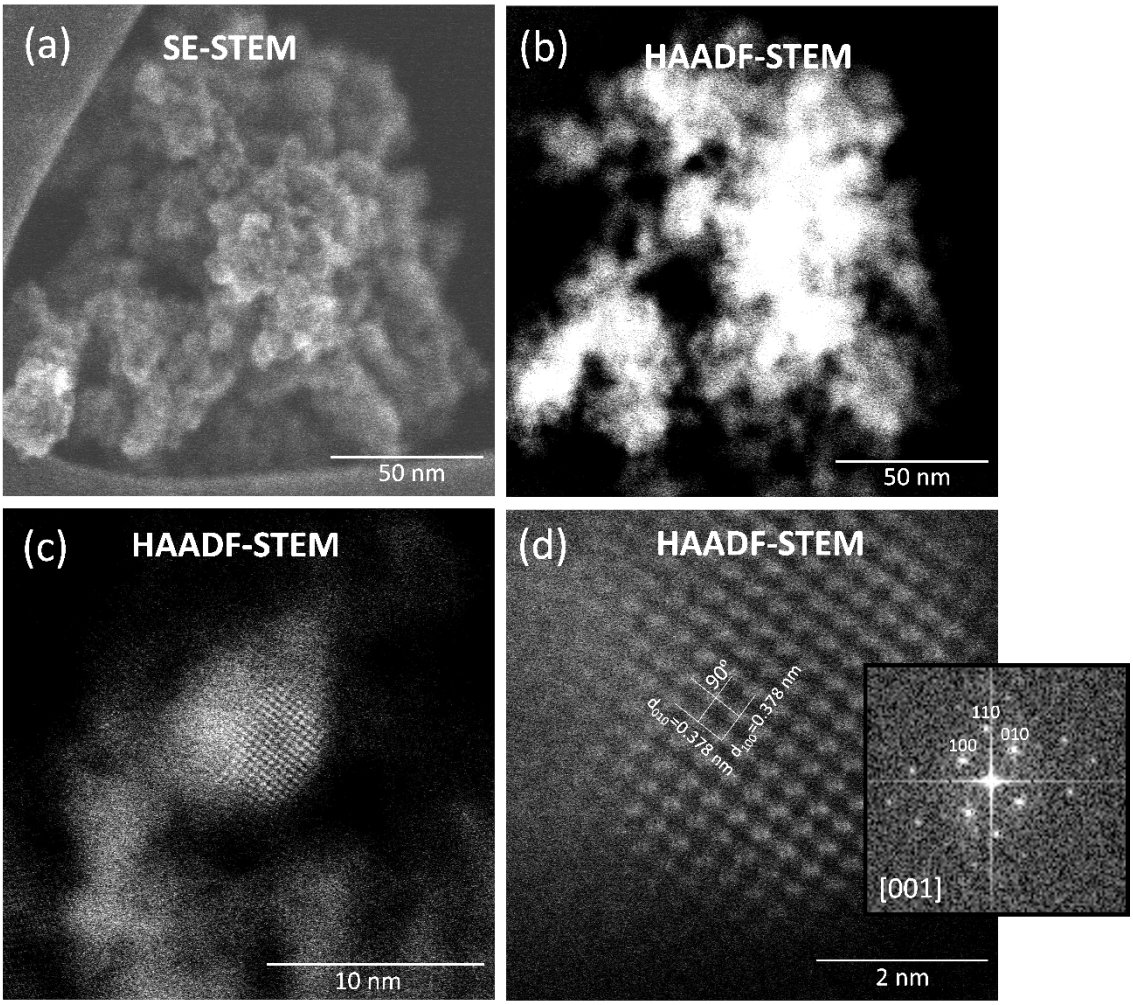

Figure 3.1.3 - (a) Secondary electron (SE) STEM image of the B2 sample, (b) HAADF image of the area in (a), (c) and (d) Magnified HAADF-STEM image of a TiO2 nanocrystal. The inset in (d) shows the FFT image of the analyzed TiO2 nanocrystal.

3.1.4 Raman

Raman spectroscopy assessments were undertaken to affirm the compositional integrity of the synthesized materials. Inspection of the Raman spectrum depicted in **Figure 3.1.4** elucidates the

presence of the characteristic TiO_2 anatase bands at 144 cm^{-1} (Eg), 198 cm^{-1} (Eg), 393 cm^{-1} (Eg), 515 cm^{-1} (B_{1g} + A_{1g}), and 636 cm^{-1} (Eg), incorporating the six Raman active modes (A_{1g} +2 B_{1g} +3 E_g) [87]. The verified purity of the resultant TiO_2 nanopowder aligns seamlessly with the corroborative XRD data, substantiating the fidelity of the synthesized material.

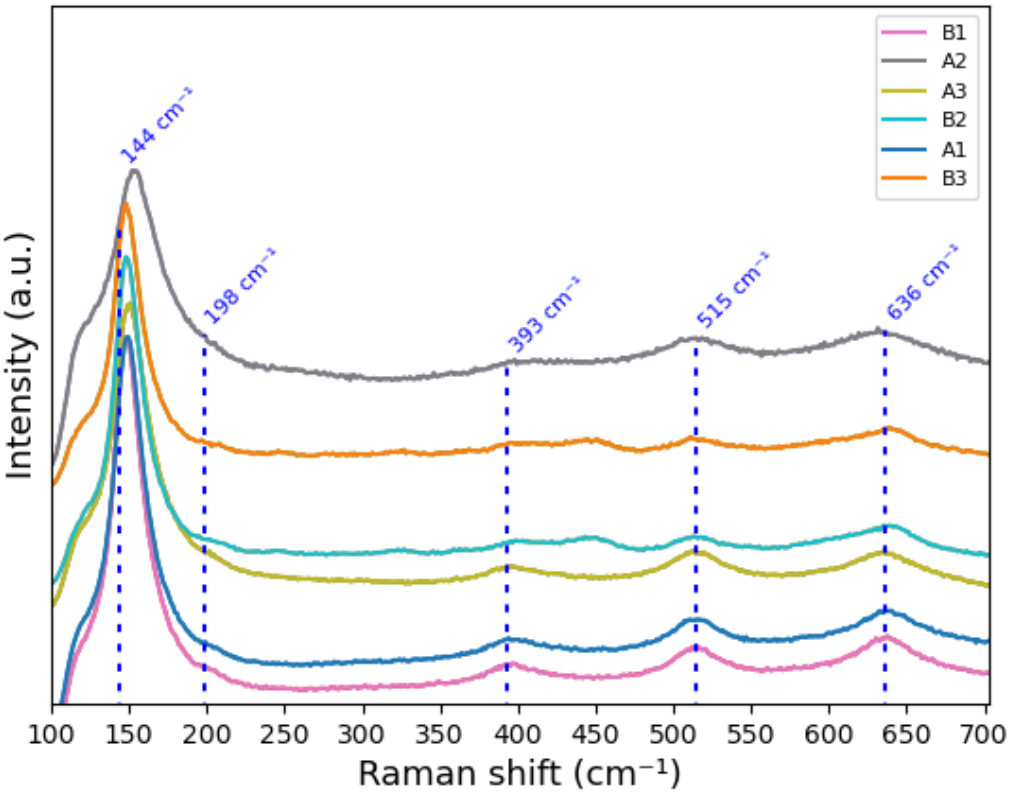

Figure 3.1.1 - Representative Raman spectrum of the synthesized TiO_2 nanopowders. The vertical dot lines represent anatase TiO_2 bands.

3.2 Optical characterization

3.2.1 Optical Band Gap

The determination of the optical band gap energy for the synthesized nanoparticles was accomplished using the Tauc method. The Tauc equation is articulated as follows:

$$(\alpha h\nu) = A(h\nu - E_g)^m \quad (1)$$

In the context of the Tauc equation, the symbols represent the following parameters: 'α' denotes the absorption coefficient, 'h' stands for the Planck constant, 'ν' represents the photon's frequency, 'A' is an energy-independent constant, 'E_g' signifies the energy band gap, and 'm' is a constant contingent

upon the nature of the electron transition—assuming a value of ½ for allowed direct transitions and 2 for allowed indirect transitions. Furthermore, the absorption spectra 'α' can be interchanged with the measured reflectance spectra 'R' by employing the Kubelka−Munk function F(R), equation:

$$F(R) = \frac{(1-R)^2}{2R} = \frac{k}{s} \tag{2}$$

In the given expression, 'R' denotes the absolute reflectance of the nanoparticles, 'k' signifies the absorption coefficient, and 's' represents the scattering coefficient. Consequently, to determine the energy band gap of the nanoparticles, both equations (equation 1 and 2) were integrated. The resultant plot of $(F(R)h\upsilon)^{1/m}$ vs $(h\upsilon)$ utilized the measured reflectance. Subsequently, the linear region of this plot was extrapolated, as illustrated in (**Figure 3.2.1.**) [88-90]. It's noteworthy that this methodology is applicable to all semiconducting materials that do not absorb light of sub-band gap energy or exhibit negligible absorbance [91].

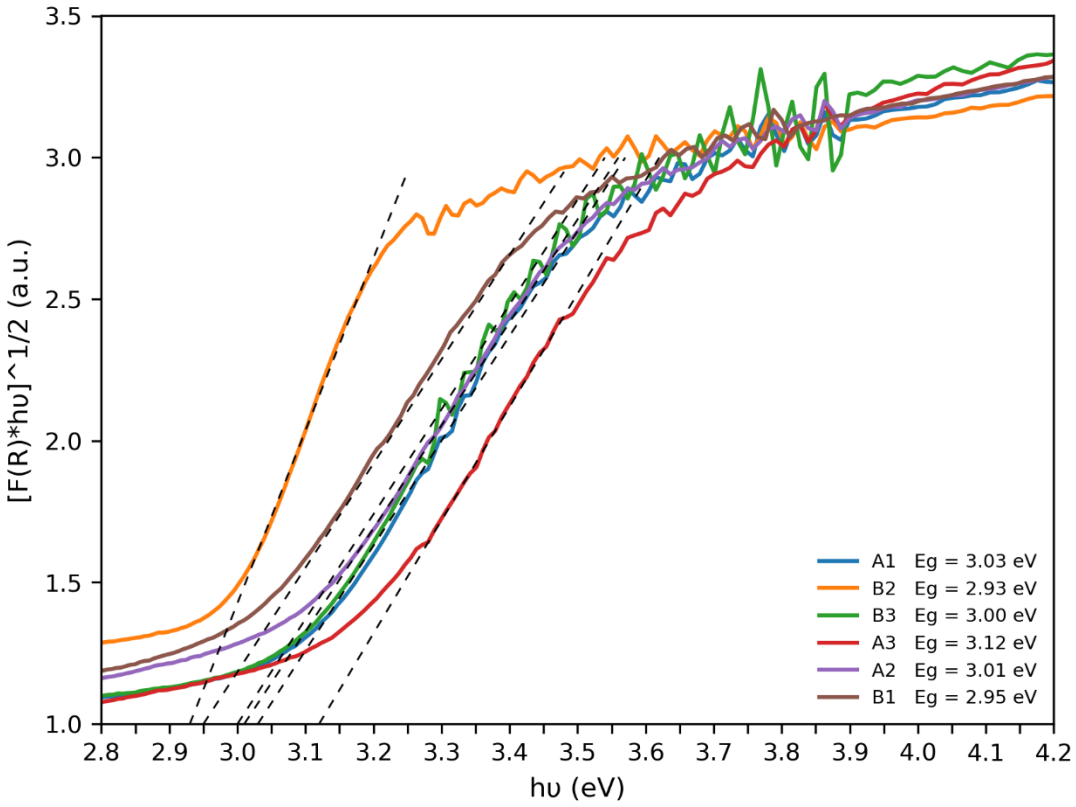

Figure 3.2.1 - Optical band gaps $(F(R)h\nu)^{1/m}$ vs $(h\nu)$ plots for TiO_2 nanostructures.

Band gap values for A1, A2, A3, B1, B2 and B3 are 3.03 eV, 3.01 eV, 3.12 eV, 2.95 eV, 2.93 eV and 3.00 eV, respectively. When analyzing the values, it is noticeable that B1, B2 and B3 all had lower band gaps than A1, A2 and A3, meaning that samples from approach B can have a better photocatalytic performance than those form approach A, just for the fact that they can absorb more visible light. One possible explanation to why approach B samples present lower band gaps is due to the presence of defects, such as oxygen vacancies. These vacancies act as electron traps, creating energy levels within the band structure of TiO_2. These vacancies can reduce the band gap energy, influencing the material's electronic properties. Additionally, the presence of vacancies can enhance photocatalytic activity by facilitating charge carrier generation and promoting redox reactions.

3.3 Morphological and structural characterization of the functional 3D printed structure

The successful integration of nanoparticles onto the surfaces of 3D printed structures was accomplished through different techniques. The figure below visually presents SEM images of the structures employing approach A with in-situ growth (**Figure 3.3.1. b, c** and **d**), approach B with the DC technique (**Figure 3.3.1. e, f** and **g**) and also an image of the 3D printed structure without nanoparticles on it (**Figure 3.3.1. a).** At first, it is noticeable the difference between the 3D structure without nanoparticles on it (**Figure 3.3.1. a)** and the rest of the images (**Figure 3.3.1. b-g**), where it can clearly be observed and identified the presence of TiO_2 nanoparticles.

When analyzing the images from approach A and approach B, some similarities can be observed between both approaches such as large agglomerates of nanoparticles that are present on the resin matrix and a complete and uniform coverage of it.

Regarding the images from approach A, which had the TiO_2 nanoparticles synthesized and grown *in-situ*, due to the 3D structure being inside the glass vessel with the solution, it is noticeable the presence of smaller particles and agglomerates of nanoparticles than the images of approach B. The essence of this technique lies in the necessity for SLA 3D printed structures to undergo a UV post-curing procedure following their emergence from the printer. This process is crucial for transforming monomers into intricately interconnected polymer networks [92]. As the curing unfolds, the structures undergo thermal expansion induced by UV light and temperature exposure [93]. Consequently, the final structures exhibit a reduction in size at room temperature while concurrently improving their mechanical properties in comparison to their pre-cured state [94-95]. Therefore, by applying a coating of nanoparticles onto the surface of the nascent, uncured structure, these nanoparticles gradually integrate into the resin during the curing process, becoming firmly affixed to the surface post-curing and subsequent cooling.

Now, with the images of approach B, it is observed larger nanoparticles and also larger agglomerates of it. This can be explained due to the fact that in this approach, the conditions set to synthesize TiO_2 nanoparticles were different than approach A, mainly in terms of temperature and pressure. Elevated temperatures provide particles with greater thermal energy, enabling them to overcome

intermolecular forces and facilitating the fusion of smaller particles into larger ones. Additionally, higher pressures compress the particles, reducing the void spaces between them and promoting particle coalescence [96]. Overall, the combination of elevated temperature and pressure promotes more vigorous molecular motion and closer proximity between particles, leading to the agglomeration and growth of particle sizes. Also, the technique used to impregnate the 3D structure was different. The particles adhere to the surface through capillary forces upon withdrawal from the solution. While (DC) may take more time due to multiple steps, including nanoparticle synthesis and coating, it offers an alternative for nanoparticle integration. Factors like solution concentration, withdrawal speed, and drying conditions impacted the size, distribution, and adhesion strength of nanoparticles, potentially leading to variations in coating uniformity and the formation of larger agglomerates of nanoparticles [97]. Nevertheless, both techniques revealed to successfully cover the surface of the 3D resin with good adhesion to Its surface.

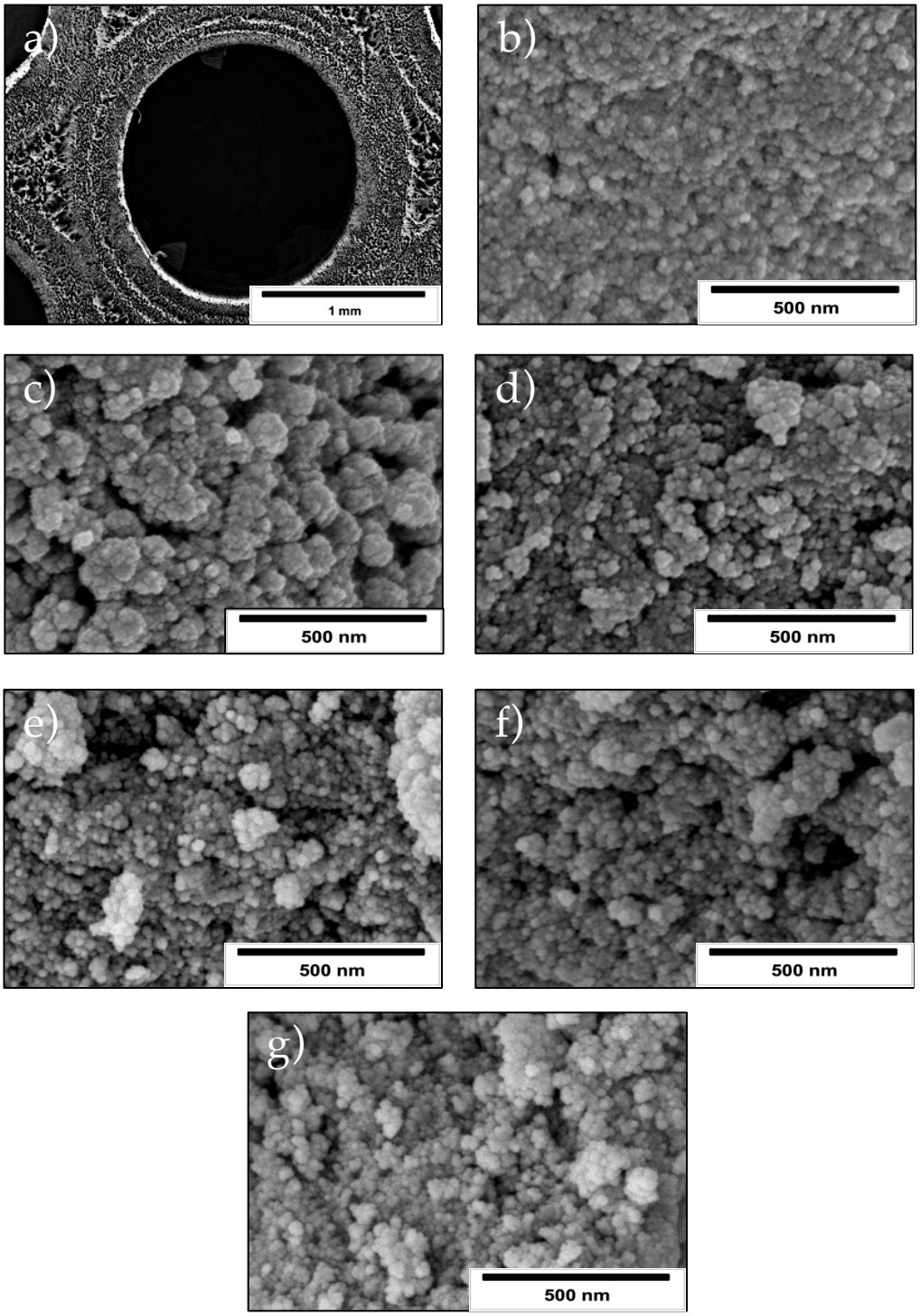

Figure 3.3.1 - SEM images of (a) the 3D structure without TiO_2 nanoparticles, (b) (c) (d) the 3D structure with TiO_2 nanoparticles incorporated via microwave irradiation (*in-situ* growth) A1, A2, A3 (respectively) and (e) (f) (g) the 3D structure with TiO_2 nanoparticles incorporated via dip coating B1, B2, B3 (respectively).

3.4 Photocatalytic activity

The photocatalytic prowess of TiO_2 under UV irradiation has been extensively explored and has yielded remarkable outcomes [98-101]. However, when exposed to sunlight, a diminished photocatalytic performance is anticipated due to TiO_2 being a wide band gap semiconductor. The solar spectrum encompasses UV (5%), visible (40%), and infrared (IR 55%) wavelengths. Yet, as TiO_2 primarily absorbs in the UV region, it selectively captures only the UV segment of the solar spectrum [7]. The variability in solar radiation intensity induced by weather, time of day, and other factors underscores the necessity for solar simulators, which enhance experimental precision and afford better control over radiation intensity. The credibility of a solar simulator is contingent upon meeting certain criteria, including high spectral match, low-irradiation spatial nonuniformity, and minimal temporal instability, in comparison to natural sunlight [102].

One structure was generated as subject of investigation. This structure consists of a circular disk with circular holes displayed in a honeycomb pattern, totalizing a surface area of 427 mm^2.

3.4.1 3D printed TiO2 photocatalysis

RhB serves as an exemplary organic compound for photocatalytic activity assessments due to its high-water solubility and an absorption peak within the visible range (554 nm), facilitating monitoring of degradation through optical absorbance spectroscopy. Not only is RhB a commonly employed chemical in industrial production, but it is also a contributor to environmental pollution. Consequently, the photocatalytic performance of TiO_2 structures was appraised by examining the degradation of RhB under sunlight simulator conditions. The outcomes are graphically presented in **Figure 3.4.1.** accompanied by the corresponding degradation percentages calculated using equation 3:

$$Degradation\ (\%) = \frac{C_o - C}{C_o}\ X\ 100 \tag{3}$$

In equation 3, 'C_o' represents the initial absorbance of the RhB solution, while 'C' denotes the absorbance of the RhB solution at each specific exposure time.

All experiments were initiated with the RhB solution at an absorbance value of 1. The tests were concluded upon the initial occurrence of a hypsochromic shift in the RhB solution.

The hypsochromic shift observed is a consequence of the self-photosensitization phenomenon of the dye when exposed to visible light. This occurrence is typical in visible light-assisted photocatalysis involving dyes [103-104]. Beyond the degradation of the dye resulting from the destruction of the chromophore structure through photocatalytic processes, RhB molecules, when exposed to visible light, can transition to an excited state. In this excited state, electrons are transferred to the CB of the photocatalyst, leading to the formation of RhB cation radicals. These cation radicals are accountable for subsequent N-de-ethylation reactions [105-107]. The gradual hypsochromic shift in the absorbance peak is attributed to the formation of N-de-ethylated products, as the N-de-ethylation of RhB is recognized to be a stepwise process [108-109]. Therefore, the appearance of the hypsochromic shift signifies that the degradation of RhB is no longer primarily attributable to the action of the photocatalyst.

The degradation of RhB utilizing 3D printed TiO_2 structures under a simulated sunlight environment yielded notable outcomes. Notably, B2 (**Figure 3.4.1.**) demonstrated the most significant efficacy, achieving an 85% degradation after 120 minutes. Following closely, B1 (**Figure 3.4.1.**) secured the second position with a 68% degradation over the same exposure duration, reflecting a discernible 25% deviation from B2. Claiming the third spot, B3 (**Figure 3.4.1.**) exhibited a 60% degradation, marking a nearly 42% reduction (almost half) in photocatalytic performance compared to B2. A2 (**Figure 3.4.1.**) occupied the subsequent position, showcasing a 35% degradation. Concluding the series, A1 (**Figure 3.4.1.**) and A3 (**Figure 3.4.1.**) registered 26% and 25% degradation, respectively.

The disparities between the results obtained from approaches A and B are noteworthy. While none of the samples from approach A attained a degradability threshold of 50%, all samples from approach B not only surpassed this benchmark but achieved a notable 60% or more in degradability. This substantiates the superiority of approach B over approach A. These findings hold great promise, especially when contrasted with existing literature, where TiO_2 photocatalysis under visible light often necessitates prolonged degradation periods. Prior studies by W. Ren et al. [110] observed almost 30% degradation over 300 minutes using undoped nanoparticles. J. Wang et al. [111] reported a 10% degradation of RhB in 25 minutes and certain investigations employing 3D printed TiO_2 structures under visible sunlight required more extensive exposure times, up to 6 hours, to achieve 75% efficiency [31].

Furthermore, the degradation ratio was assessed using the Langmuir-Hinshelwood (L-H) kinetic model. For the pseudo first-order reaction, the L-H model equation is expressed as follows:

$$-dC/dt = kC \tag{4}$$

where C is the concentration, k is the rate constant, and t is the time.

The rate constant k can be determined from the slope of the linear fitted line by plotting the pseudo first-order reaction using the equation:

$$\ln(C_o/C) = kt \tag{5}$$

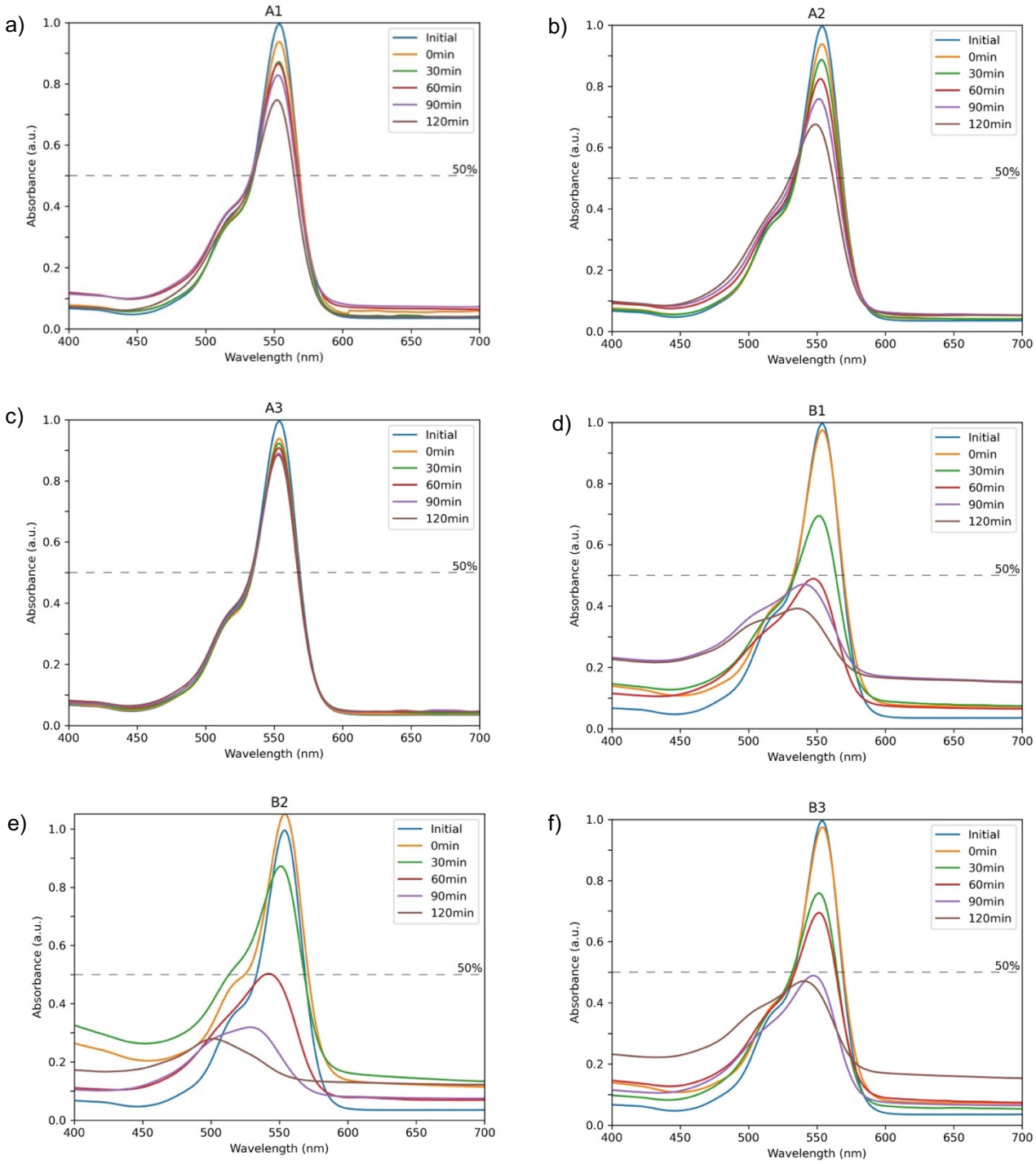

Figure 3.4.1- RhB absorbance spectra under sunlight simulator conditions (led Simulator with AM 1.5 spectrum) (a) A1, (b) A2, (c) A3, (d) B1, (e) B2 and (f) B3

The degradation ratio vs time of exposure are displayed in **Figure 3.4.2.** A 3D structure without TiO_2 present in it was exposed in RhB under solar simulator conditions (Resin_RhB). The findings suggest that the resin lacks inherent photocatalytic properties, and the entirety of the degradation observed is attributed solely to the influence of nanoparticles integrated into the surface (**Figure 3.4.2.**). To facilitate a quantitative comparison, rate constants were computed to serve as indicators of the respective photoactivities.

The photocatalyst exhibiting the highest performance was B2, registering a constant rate of 0.0174 min^{-1}, followed by B1 at 0.0092 min^{-1}, and B3 with a rate of 0.0075 min^{-1}. In contrast, samples from approach A demonstrated notably lower constant rates, specifically 0.0036 min^{-1} for A2 and 0.022 min^{-1} for A1. A3 emerged as the least efficient photocatalyst, recording a rate of 0.0010 min^{-1}.

Through a comprehensive analysis of each incorporation method in terms of photocatalytic performance, it becomes evident that an additional enhancement in the degradation rate is achieved when structures with impregnated nanoparticles are synthesized under the conditions of approach B.

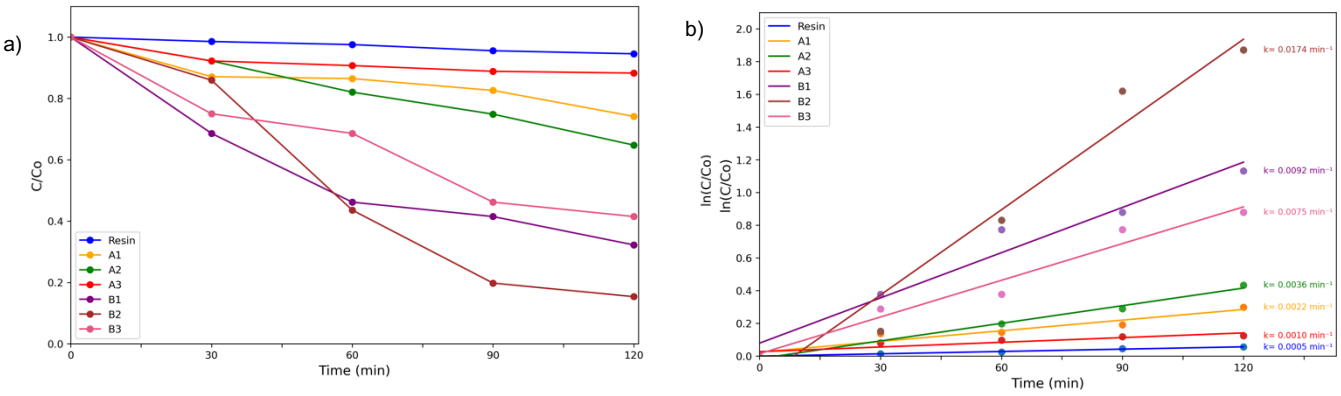

Figure 3.4.2 - (a) RhB degradation ratio (C/C_0) vs. exposure time for the 3D printed TiO_2 structures under light simulator (b) Kinetic parameters of the structures with the respective fit curves.

As previously elucidated, the photocatalytic efficacy of semiconductor materials is intricately governed by various determinants crystallinity, encompassing band gap energy, surface defects, nanostructure crystal facets, and high surface area, among other factors. In this specific instance, the photocatalytic performance was distinctly influenced by the method employed for nanoparticle synthesis conditions. This is underscored by the fact that all TiO_2 nanostructures exhibited uniform characteristics, notably being of the anatase phase, characterized by a substantial effective surface area conducive to heightened surface reactions. Additional shared attributes included an optical band gap below 3.12 eV.

The enhancement observed in the constant rates from approach A to approach B can be attributed to the increased temperature and pressure during (MW) synthesis.

The superior efficacy of ethanol as a solvent in the synthesis of TiO_2 nanoparticles via (MW) irradiation, leading to enhanced photocatalytic performance, can be attributed to several factors. (MW) radiation interacts with the solution molecules, converting energy from electromagnetic into thermal [112]. Hence, it can be deduced that the selection of diverse solvents holds significance in organic synthesis. Among the crucial factors influencing (MW) synthesis, solvent polarity stands out as a key parameter. As solution polarity rises, the heating process becomes more effective due to enhanced interaction with (MW) energy [113]. The viscosity of a solvent is a crucial factor that influences its capacity to absorb (MW) energy, primarily impacting molecular rotation. In highly viscous mediums, molecular mobility is constrained, making it challenging for molecules to align with electromagnetic radiation. Consequently, the heat generated through dipole rotation decreases in such environments [114].

Ethanol, characterized by its unique chemical properties, facilitates a homogeneous and efficient reaction environment. Its relatively low boiling point ensures rapid evaporation during (MW) irradiation, promoting the formation of nanoparticles with desirable characteristics. Additionally, ethanol's excellent solvating power enables the dissolution of titanium precursor compounds, fostering uniform dispersion and promoting the formation of well-defined nanoparticles. The controlled interaction between ethanol and titanium precursors likely influences the nucleation and growth processes, contributing to the synthesis of TiO_2 nanoparticles with optimal size, morphology, and crystalline structure. Moreover, the distinctive properties of ethanol, such as its ability to act as a reducing agent, may play a role in governing the reduction-oxidation dynamics during the synthesis, influencing the final characteristics of the TiO_2 nanoparticles [115-118]. The synergistic effects of these factors collectively contribute to the superior photocatalytic performance observed in TiO_2 nanoparticles synthesized using ethanol as the solvent under (MW) irradiation.

There are a lot of factors that have an influence in TiO_2 photocatalytic behavior like the specific surface area, the crystalline phase and particle size [119-120]. Larger particles are known to have a lower surface-to-volume ratio and specific surface area [34]. Despite this, spheres were also seen, which increased the number of active sites available for photocatalytic processes. According to STEM, one of the most active surfaces for photocatalysis in TiO_2 is the (100) surface, which was exposed in TiO_2 nanocrystals. This is because it has a greater electronic band structure and a superior surface atomic structure with 100% five-coordinate Ti atoms (Ti_{5c}). This allows for the generation of higher reductive and oxidative photoexcited charge carriers, which are then transferred to the TiO_2 surface to react with the pollutant molecules and increase photocatalytic performance [121-122].

Hierarchically mesoporous TiO_2 nanostructures demonstrate exceptional photocatalytic efficacy due to their substantial surface area, enabling the adsorption of reactant molecules on numerous active sites and large pore volumes facilitating the diffusion of pollutant molecules during the photocatalysis reaction. This attribute is advantageous for reaction kinetics [62]. Consequently, quantum sized mesoporous TiO_2 exhibits more efficient separation of photogenerated charge carriers, indicative of robust redox reactions [123-124].

3.4.1.1 Reusability test

A crucial consideration for practical applications is the reusability of the photocatalyst, contributing not only to the recovery of the photocatalyst but also to the viability of water treatment at an industrial scale. Therefore, a three-cycle test was conducted for the DC B2 sample (**Figure 3.4.3.**). After each cycle, the photocatalyst was washed with water, exposed under UV light for 30 minutes each side to clean residues, and reintroduced into a container with a new RhB solution. The photodegradation of RhB for the three cycles and the degradation rate are depicted in **Figure 3.4.3.**, respectively.

As illustrated in **Figure 3.4.3.**, the degradation curves are remarkably different. The first exposure exhibits degradation with a rate constant (k) of 0.0060 min^{-1}, the second exposure with k = 0.0023 min^{-1}, and the third exposure with k = 0.0015 min^{-1}. This inconsistency demonstrates crucial problems in the reusability properties of the sample, since its performance plummets.

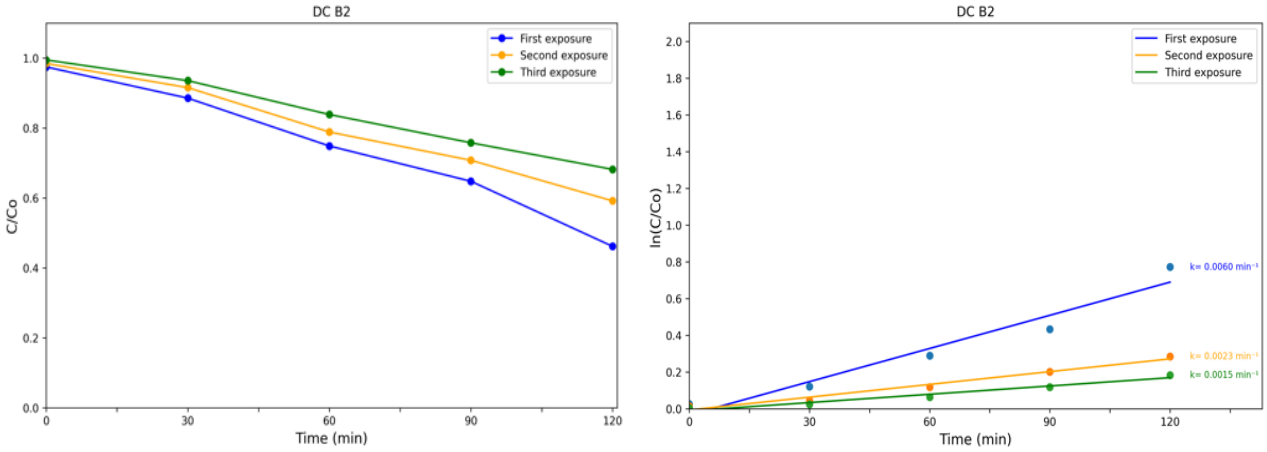

Figure 3.4.3 - (a) Different cycles of RhB degradation ratio (C/C_0) vs. exposure time for DC B2 structure under sunlight simulator. (b) Kinetic parameters of the structures, with the respective fit curves.

Following a thorough analysis of the preceding experimental outcomes, the reasons behind the underwhelming performance observed in the reusability test during successive photocatalytic trials, were unknown. A revelation emerged during a meticulous examination under the scanning electron microscope (SEM), giving a sense of disappointment. **Figure 3.4.4**. starkly illustrates observable cracks on the TiO_2 film, unveiling an undisclosed factor contributing to the challenges faced in replicating the test.

This discovery underscores the pivotal role of viscosity control in the deposition process of TiO_2 films utilizing the sol-gel (DC) technique. Citing existing research, the highlighted passage emphasizes the critical management of parameters such as ionic concentration, heating conditions, and withdrawal speed to ensure the production of crack-free films [125]. The emergence of cracks becomes apparent when thin films reach a critical thickness [126]. Notably, the regulation of withdrawal speed proves instrumental in preventing crack and bubble formation post-annealing [127].

Furthermore, the sol-gel (DC) technique provides a versatile means of manipulating the film's microstructure by adjusting solution composition and deposition conditions. This, in turn, influences the

achievement of crack-free TiO_2 thin films [128]. This connection elucidates the intricate interplay of deposition conditions and their consequential impact on crack formation in TiO_2 thin films.

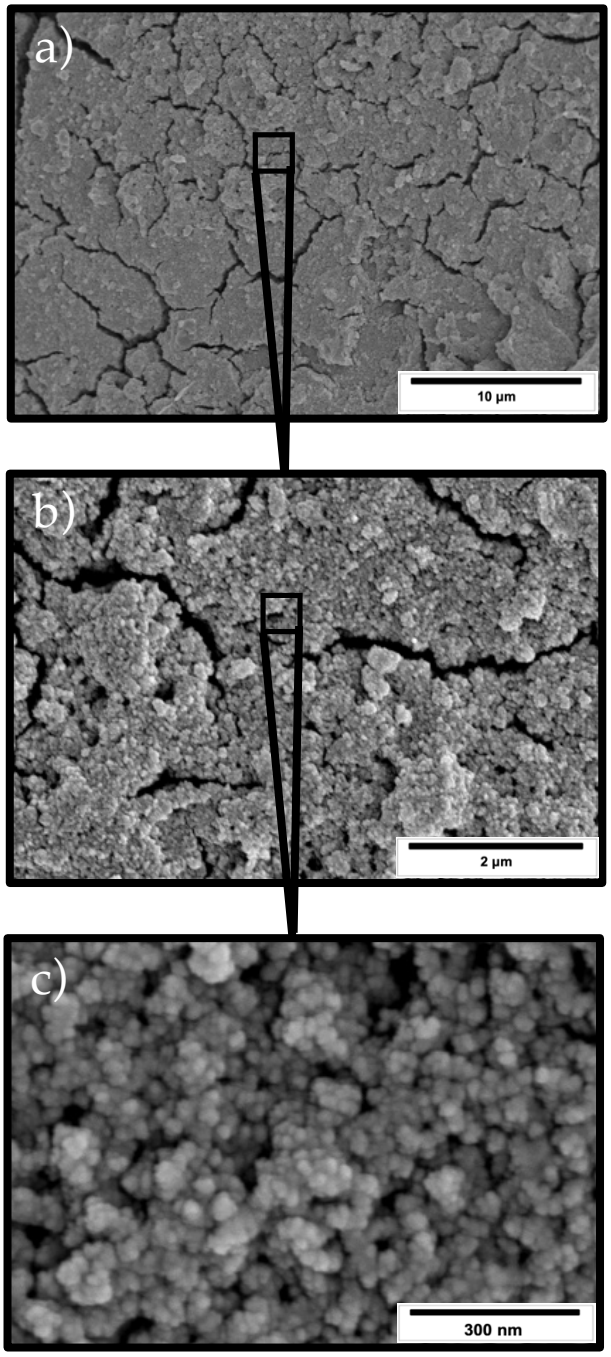

Figure 3.4.4 - SEM images of the surface of the 3D printed TiO_2 structure DC B2 after 3 exposures to under sunlight simulator conditions

3.4.1.2 Photocatalysis under natural sunlight

As a proof of concept, photocatalytic activity at natural sunlight conditions was performed for DC B2 and the following result is shown in **Figure 3.4.5**. The degradation rate of RhB was 0.0062 min^{-1}, which was much lower compared to the sun simulator exposure, mainly due to the low and oscillating UV index and the atmospherical conditions.

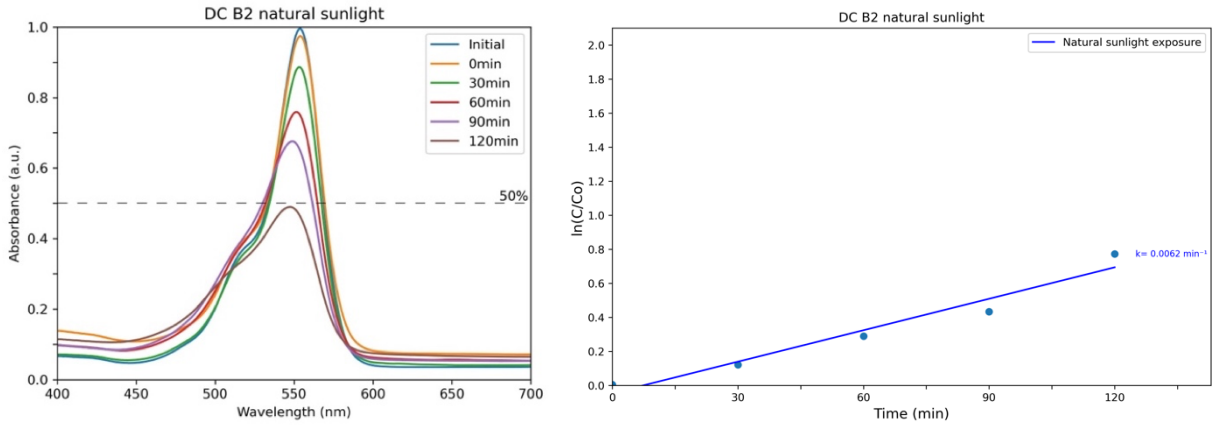

Figure 3.4.5 - (a) RhB degradation ratio (C/C_0) vs. exposure time for DC B2 structure under natural sunlight. (b) Kinetic parameters of the structure, with the respective fit curve.

4

CONCLUSION AND FUTURE PERSPECTIVES

In conclusion, the comprehensive investigation into the synthesis, 3D printing, and photocatalytic performance of TiO_2 nanostructures has yielded valuable insights. The successful integration of nanoparticles onto 3D printed structures using *in-situ* growth and (DC) approaches showcased distinctive characteristics, with approach B consistently demonstrating superior performance in terms of photocatalytic activity.

Structural analysis through SEM, STEM, XRD, and Raman spectroscopy confirmed the successful synthesis of TiO_2 nanoparticles with a macro-mesoporous structure. The utilization of (MW) irradiation for nanoparticle synthesis, followed by SLA 3D printing, proved effective, highlighting the potential for scalable and precise manufacturing.

Photocatalytic assessments, particularly under sunlight simulator conditions, emphasized the considerable impact of synthesis conditions on the photocatalytic efficiency of TiO_2 structures.

Reusability assessments, although presenting challenges, provided crucial insights into the limitations of dip-coated samples, specifically B2, attributed to crack formation in the TiO_2 film. This underscores the importance of meticulous control over deposition conditions, particularly viscosity, in enhancing the long-term stability and performance of TiO_2-based photocatalysts.

Looking ahead, future research endeavors should focus on addressing the identified challenges, such as crack formation during the (DC) process. Exploring advanced deposition techniques and optimizing synthesis conditions could contribute to enhancing the reusability and scalability of TiO_2-based photocatalysts. Additionally, the environmental impact of the photocatalytic process and the potential release of by-products should be thoroughly investigated to ensure the sustainability of water treatment solutions.

The integration of 3D printing with advanced photocatalytic materials opens avenues for innovative applications in water treatment and beyond. This study highlights the need for continued interdisciplinary collaboration between material scientists, engineers, and environmental researchers to propel the development of efficient, cost-effective, and sustainable water purification technologies. The fusion of 3D printing and photocatalysis represents a promising approach for addressing global water challenges, providing cleaner and accessible water resources for future generations.

REFERENCES

[1] Nunes, D., et al. "Enhanced UV flexible photodetectors and photocatalysts based on TiO 2 nanoplatforms." *Topics in Catalysis* 61 (2018): 1591-1606.

[2] Sahu, Kirti, Mahesh Dhonde, and Vemparala Venkata Satyanarayana Murty. "Microwave-assisted hydrothermal synthesis of Cu-doped TiO2 nanoparticles for efficient dye-sensitized solar cell with improved open-circuit voltage." *International Journal of Energy Research* 45.4 (2021): 5423-5432.

[3] Nunes, Daniela, et al. "TiO2 nanostructured films for electrochromic paper based-devices." *Applied Sciences* 10.4 (2020): 1200.

[4] Nakata, Kazuya, and Akira Fujishima. "TiO2 photocatalysis: Design and applications." *Journal of photochemistry and photobiology C: Photochemistry Reviews* 13.3 (2012): 169-189.

[5] Cedillo-González, Erika Iveth, et al. "Self-cleaning glass prepared from a commercial TiO2 nano-dispersion and its photocatalytic performance under common anthropogenic and atmospheric factors." *Building and Environment* 71 (2014): 7-14.

[6] Nunes, Daniela, Elvira Fortunato, and Rodrigo Martins. "Flexible nanostructured TiO2-based gas and UV sensors: A review." *Discover Materials* 2.1 (2022): 2.

[7] Rajbongshi, Biju Mani. "Photocatalyst: mechanism, challenges, and strategy for organic contaminant degradation." *Handbook of Smart Photocatalytic Materials*. Elsevier, 2020. 127-149.

[8] Lan, Yucheng, Yalin Lu, and Zhifeng Ren. "Mini review on photocatalysis of titanium dioxide nanoparticles and their solar applications." *Nano energy* 2.5 (2013): 1031-1045.

[9] Katal, Reza, et al. "A review on the synthesis of the various types of anatase TiO2 facets and their applications for photocatalysis." *Chemical Engineering Journal* 384 (2020): 123384.

[10] Li, Gonghu, and Kimberly A. Gray. "The solid–solid interface: Explaining the high and unique photocatalytic reactivity of TiO2-based nanocomposite materials." *Chemical physics* 339.1-3 (2007): 173-187.

[11] Du, Yi-en, et al. "Microwave-assisted synthesis of high-energy faceted TiO2 nanocrystals derived from exfoliated porous metatitanic acid nanosheets with improved photocatalytic and photovoltaic performance." *Materials* 12.21 (2019): 3614.

[12] Bokare, Anuja, and Folarin Erogbogbo. "Photocatalysis and Li-Ion Battery Applications of {001} Faceted Anatase TiO2-Based Composites." *J* 4.3 (2021): 500-530.

[13] Selloni, Annabella. "Anatase shows its reactive side." *Nature Materials* 7.8 (2008): 613-615.

[14] Liu, Gang, et al. "Enhanced photoactivity of oxygen-deficient anatase TiO2 sheets with dominant {001} facets." *The Journal of Physical Chemistry C* 113.52 (2009): 21784-21788.

[15] Nunes, Daniela, et al. "Photocatalytic behavior of TiO2 films synthesized by microwave irradiation." *Catalysis Today* 278 (2016): 262-270.

[16] Xu, Chengkun, et al. "Photocatalytic effect of carbon-modified n-TiO2 nanoparticles under visible light illumination." *Applied Catalysis B: Environmental* 64.3-4 (2006): 312-317.

[17] Cong, Ye, et al. "Carbon-doped TiO2 coating on multiwalled carbon nanotubes with higher visible light photocatalytic activity." *Applied Catalysis B: Environmental* 107.1-2 (2011): 128-134.

[18] Wu, Zhongbiao, et al. "The fabrication and characterization of novel carbon doped TiO2 nanotubes, nanowires and nanorods with high visible light photocatalytic activity." *Nanotechnology*20.23 (2009): 235701.

[19] Yang, Xi-jia, et al. "Preparation and photocatalytic performance of Cu-doped TiO2 nanoparticles." *Transactions of Nonferrous Metals Society of China* 25.2 (2015): 504-509.

[20] Zhou, Wenfang, et al. "Preparation and properties of vanadium-doped TiO2 photocatalysts." *Journal of Physics D: Applied Physics* 43.3 (2010): 035301.

[21] Zhou, Minghua, et al. "Preparation and photocatalytic activity of Fe-doped mesoporous titanium dioxide nanocrystalline photocatalysts." *Materials Chemistry and Physics* 93.1 (2005): 159-163.

[22] Barakat, M. A., et al. "Photocatalytic degradation of 2-chlorophenol by Co-doped TiO2 nanoparticles." *Applied Catalysis B: Environmental* 57.1 (2005): 23-30.

[23] de Oliveira, Carlos Rafael Silva, et al. "Synthesis of superacid sulfated TiO2 prepared by sol-gel method and its use as a titania precursor in obtaining a kaolinite/TiO2 nano-hybrid composite." *Powder Technology* 381 (2021): 366-380.

[24] Dibenedetto, Carlo Nazareno, et al. "PbS Quantum Dots Decorating TiO2 Nanocrystals: Synthesis, Topology, and Optical Properties of the Colloidal Hybrid Architecture." *Molecules* 25.12 (2020): 2939.

[25] Wang, Zhinuo, et al. "Preparation and characterization of TiO2 nanoparticles by two different precipitation methods." *Ceramics International* 46.10 (2020): 15333-15341.

[26] Wu, Zhi Gang, et al. "Hydrothermal synthesis of TiO2 quantum dots with mixed titanium precursors." *Separation and Purification Technology* 251 (2020): 117328.

[27] Nunes, Daniela, et al. "Ultrafast Microwave Synthesis of WO3 Nanostructured Films for Solar Photocatalysis." *physica status solidi (RRL)–Rapid Research Letters* 15.9 (2021): 2100196.

[28] Yang, Guijun, and Soo-Jin Park. "Conventional and microwave hydrothermal synthesis and application of functional materials: A review." *Materials* 12.7 (2019): 1177.

[29] Nunes, Daniela, et al. "Photocatalytic behavior of TiO2 films synthesized by microwave irradiation." *Catalysis Today* 278 (2016): 262-270.

[30] Matias, Maria Leonor, et al. "The Effect of Iron on TiO2 Nanostructures Deposited on Porous Platforms for Water Purification." *Materials Proceedings* 8.1 (2022): 146.

[31] Xue, Rita. *3D printed TiO2 nanostructures for water purification using sunlight*. Diss. 2021.

[32] Wu, Xing, et al. "Synthesis of titania nanotubes by microwave irradiation." *Solid state communications* 136.9-10 (2005): 513-517.

[33] Mahmood, Mohammad Abbas, and Joydeep Dutta. "Microwave assisted hydrothermal synthesis of zinc hydroxystannate films on glass substrates." *Journal of sol-gel science and technology* 62 (2012): 495-504.

[34] Matias, Maria Leonor, et al. "Floating TiO2-Cork Nano-Photocatalysts for Water Purification Using Sunlight." *Sustainability* 14.15 (2022): 9645.

[35] Al-Etaibi, Alya M., and Morsy Ahmed El-Apasery. "Microwave-assisted synthesis of azo disperse dyes for dyeing polyester fabrics: Our contributions over the past decade." *Polymers* 14.9 (2022): 1703.

[36] Ding, Kuan, et al. "Catalytic microwave-assisted pyrolysis of plastic waste over NiO and HY for gasoline-range hydrocarbons production." *Energy Conversion and Management* 196 (2019): 1316-1325.

[37] Tang, Zhe, et al. "Microwave-assisted synthesis of uranium doped Y2Zr2O7 transparent ceramics as potential near-infrared optical lens." *Scripta Materialia* 178 (2020): 90-93.

[38] Li, Shu-Ming, et al. "Cellulose–silver nanocomposites: Microwave-assisted synthesis, characterization, their thermal stability, and antimicrobial property." *Carbohydrate polymers* 86.2 (2011): 441-447.

[39] Negishi, Nobuaki, Koji Takeuchi, and Takashi Ibusuki. "Preparation of the TiO2 thin film photocatalyst by the dip-coating process." *Journal of Sol-Gel Science and Technology* 13.1-3 (1998): 691-694.

[40] Thongsuriwong, K., P. Amornpitoksuk, and S. Suwanboon. "Structure, morphology, photocatalytic and antibacterial activities of ZnO thin films prepared by sol–gel dip-coating method." *Advanced Powder Technology* 24.1 (2013): 275-280.

[41] Sonawane, R. S., S. G. Hegde, and M. K. Dongare. "Preparation of titanium (IV) oxide thin film photocatalyst by sol–gel dip coating." *Materials chemistry and physics* 77.3 (2003): 744-750.

[42] Yuan, Junjie, Siyu Yan, and Xiong Zhang. "Superhydrophilic antifogging broadband antireflective coatings with worm-like nanostructures fabricated by one dip-coating method and calcination." *Applied Surface Science* 506 (2020): 144795.

[43] Kayani, Zohra Nazir, et al. "Assessment of antibacterial and optical features of sol-gel dip coated La doped TiO2 thin films." *Materials Chemistry and Physics* 250 (2020): 123217.

[44] Zhao, Sikai, et al. "Highly selective NO2 sensor based on p-type nanocrystalline NiO thin films prepared by sol–gel dip coating." *Ceramics International* 44.1 (2018): 753-759.

[45] Gomaa, Mahmoud, Abeer Salah, and Gamal Abdel Fattah. "Utilizing dip-coated graphene/nanogold to enhance SPR-based fiber optic sensor." *Applied Physics A* 128 (2022): 1-12.

[46] Muthukrishnan, Karthika, et al. "Highly selective acetaldehyde sensor using sol–gel dip coated nano crystalline TiO 2 thin film." *Journal of Materials Science: Materials in Electronics* 26 (2015): 5135-5139.

[47] Liu, Zhiying, et al. "SMALL-hysteresis thin-film transistors achieved by facile dip-coating of nanotube/polymer composite." *Advanced Materials* 24.27 (2012): 3633-3638.

[48] Sathish, S., B. Chandar Shekar, and R. Sathyamoorthy. "Nano polymer films by fast dip coating method for field effect transistor applications." *Physics procedia* 49 (2013): 166-176.

[49] Baudry, Paul, et al. "Dip-coated TiO2 CeO2 films as transparent counter-electrode for transmissive electrochromic devices." *Journal of Non-Crystalline Solids* 121.1-3 (1990): 319-322.

[50] Catauro, Michelina, et al. "PEG-based organic–inorganic hybrid coatings prepared by the sol–gel dip-coating process for biomedical applications." *Polymer Engineering & Science* 57.6 (2017): 478-484.

[51] Liang, Ling, et al. "Optimization of dip-coating methods for the fabrication of coated microneedles for drug delivery." *Journal of Drug Delivery Science and Technology* 55 (2020): 101464.

[52] de Castro Braga, Antonio Vitor, et al. "The influence of heat treatment of inorganic conversion coatings produced by sol-gel dip coating on the anticorrosive properties of alumina films deposited on steel substrate–Part I: Single conversion coatings." *Surface and Coatings Technology* 372 (2019): 190-200.

[53] Wu, Linda YL, et al. "Adhesion enhancement of sol–gel coating on polycarbonate by heated impregnation treatment." *Thin Solid Films* 517.17 (2009): 4850-4856.

[54] Rebia, Rina Afiani, Kaho Shizukuishi, and Toshihisa Tanaka. "Characteristic changes in PHBH isothermal crystallization monofilaments by the effect of heat treatment and dip-coating in various solvents." *European Polymer Journal* 134 (2020): 109808.

[55] Butt, Muhammad A. "Thin-film coating methods: A successful marriage of high-quality and cost-effectiveness—A brief exploration." *Coatings* 12.8 (2022): 1115.

[56] Innocenzi, P. C., et al. "Coating of metals by the sol-gel dip-coating method." *Journal of the European Ceramic Society* 10.6 (1992): 431-436.

[57] Asri, R. I. M., et al. "A review of hydroxyapatite-based coating techniques: Sol–gel and electrochemical depositions on biocompatible metals." *Journal of the mechanical behavior of biomedical materials* 57 (2016): 95-108.

[58] Molaire, Michel Frantz. "A semi-empirical model for dip coating: thickness and thickness uniformity control." *NIP & Digital Fabrication Conference*. Vol. 21. Society of Imaging Science and Technology, 2005.

[59] Cisneros-Zevallos, L., and J. M. Krochta. "Dependence of coating thickness on viscosity of coating solution applied to fruits and vegetables by dipping method." *Journal of Food Science*68.2 (2003): 503-510.

[60] Nunes, Daniela, et al. "Photocatalytic behavior of TiO2 films synthesized by microwave irradiation." *Catalysis Today* 278 (2016): 262-270.

[61] Nunes, Daniela, et al. "Metal oxide-based photocatalytic paper: A green alternative for environmental remediation." *Catalysts* 11.4 (2021): 504.

[62] Zhang, Wei, et al. "Recent advances in the synthesis of hierarchically mesoporous TiO2 materials for energy and environmental applications." *National Science Review* 7.11 (2020): 1702-1725.

[63] Zhao, Zhi, Xiaoxiao Tian, and Xiaoyan Song. "Engineering materials with light: Recent progress in digital light processing based 3D printing." *Journal of Materials Chemistry C* 8.40 (2020): 13896-13917.

[64] Tumbleston, John R., et al. "Continuous liquid interface production of 3D objects." *Science* 347.6228 (2015): 1349-1352.

[65] Mendez-Arriaga, Fabiola, et al. "TiO2 3D structures for environmental purposes by additive manufacturing: Photoactivity test and reuse." *Materials Science in Semiconductor Processing*100 (2019): 35-41.

[66] Li, Nannan, et al. "Review of 3D printing in photocatalytic substrates and catalysts." *Materials Today Energy* (2022): 101100.

[67] Mendez-Arriaga, Fabiola, et al. "TiO2 3D structures for environmental purposes by additive manufacturing: Photoactivity test and reuse." *Materials Science in Semiconductor Processing*100 (2019): 35-41.

[68] Xu, Chenyang, et al. "3D Printing of Powder-Based Inks into Functional Hierarchical Porous TiO2 Materials." *Advanced Engineering Materials* 22.3 (2020): 1901088.

[69] Soundararajan, R., et al. "Appraisal of mechanical and tribological properties on PA6-TiO2 composites through fused deposition modelling." *Materials Today: Proceedings* 18 (2019): 2394-2402.

[70] Mendez-Arriaga, Fabiola, et al. "TiO2 3D structures for environmental purposes by additive manufacturing: Photoactivity test and reuse." *Materials Science in Semiconductor Processing*100 (2019): 35-41.

[71] Kozlov, D. A., et al. "Stereolithography 3D printing from suspensions containing titanium dioxide." *Russian Journal of Inorganic Chemistry* 65 (2020): 1958-1964.

[72] Aguirre-Cortés, Jhon Mauricio, et al. "3D printing in photocatalysis: Methods and capabilities for the improved performance." *Applied Materials Today* 32 (2023): 101831.

[73] Xue, Yongtao, et al. "Immobilization of photocatalytic materials for (waste) water treatment using 3D printing technology–advances and challenges." *Environmental Pollution* 316 (2023): 120549.

[74] Mai, Zhirui, et al. "Fabrication and application of photocatalytic composites and water treatment facility based on 3d printing technology." *Polymers* 13.13 (2021): 2196.

[75] Li, Nannan, et al. "Review of 3D printing in photocatalytic substrates and catalysts." *Materials Today Energy* (2022): 101100.

[76] Bai, Shen-wei, et al. "3D printing assemble technology toward advanced photocatalysis." *Materials Today Nano* (2023): 100385.

[77] Xue, R., et al. "Photocatalytic Activity of 3D Printed TiO2 Architectures Under Solar Radiation." *Photocatalysis for Environmental Remediation and Energy Production: Recent Advances and Applications*. Cham: Springer International Publishing, 2023. 79-100.

[78] McQueen, Andrew D., et al. "Photocatalytic degradation of polycyclic aromatic hydrocarbons in water by 3D printed TiO2 composites." *ACS ES&T Water* 2.1 (2021): 137-147.

[79] Bergamonti, Laura, et al. "3D printed chitosan scaffolds: A new TiO2 support for the photocatalytic degradation of amoxicillin in water." *Water research* 163 (2019): 114841.

[80] Ávila-López, Manuel Alejandro, et al. "Photodegradation of Air and Water Contaminants Using 3D-Printed TiO2 Nanoparticle Scaffolds." *ACS Applied Nano Materials* 5.8 (2022): 11437-11446.

[81] Do, Huy Hoang, et al. "Controllable fabrication of photocatalytic TiO2 brookite thin film by 3D-printing approach for dyes decomposition." *Journal of Water Process Engineering* 43 (2021): 102319.

[82] Yu, Jiaguo, et al. "Effects of acidic and basic hydrolysis catalysts on the photocatalytic activity and microstructures of bimodal mesoporous titania." *Journal of Catalysis* 217.1 (2003): 69-78.

[83] Formlabs, “High Temp resin datasheet,” pp. 0–3, 2021, [Online]. Available: https://formlabs-media.formlabs.com/datasheets/High_Temp_Technical.pdf.

[84] DeRita, Leo, et al. "Structural evolution of atomically dispersed Pt catalysts dictates reactivity." *Nature materials* 18.7 (2019): 746-751.

[85] DeRita, Leo, et al. "Structural evolution of atomically dispersed Pt catalysts dictates reactivity." *Nature materials* 18.7 (2019): 746-751.

[86] Wojcieszak, Damian, et al. "An impact of the copper additive on photocatalytic and bactericidal properties of TiO2 thin films." *Mater. Sci. Pol* 35 (2017): 421-426.

[87] El-Deen, S. S., et al. "Anatase TiO 2 nanoparticles for lithium-ion batteries." *Ionics* 24 (2018): 2925-2934.

[88] Khalil, Munawar, et al. "The influence of plasmonic Au nanoparticle integration on the optical bandgap of anatase Tio2 nanoparticles." *Int. J. Technol* 10.808.10 (2019): 14716.

[89] Aydın, C., et al. "Determination of optical band gap of ZnO: ZnAl 2 O 4 composite semiconductor nanopowder materials by optical reflectance method." *Journal of Electroceramics* 31 (2013): 265-270.

[90] Rovisco, Ana, et al. "Shape effect of zinc-tin oxide nanostructures on photodegradation of methylene blue and rhodamine B under UV and visible light." *ACS Applied Nano Materials* 4.2 (2021): 1149-1161.

[91] Makuła, Patrycja, Michał Pacia, and Wojciech Macyk. "How to correctly determine the band gap energy of modified semiconductor photocatalysts based on UV–Vis spectra." *The journal of physical chemistry letters* 9.23 (2018): 6814-6817.

[92] Decker, Christian. "UV-radiation curing chemistry." *Pigment & resin technology* 30.5 (2001): 278-286.

[93] Shardakov, Igor N., and Aleksandr N. Trufanov. "Identification of the temperature dependence of the thermal expansion coefficient of polymers." *Polymers* 13.18 (2021): 3035.

[94] Uzcategui, Asais Camila, et al. "Understanding and improving mechanical properties in 3D printed parts using a dual-cure acrylate-based resin for stereolithography." *Advanced engineering materials* 20.12 (2018): 1800876.

[95] Martín-Montal, Jordi, Jesus Pernas-Sánchez, and David Varas. "Experimental characterization framework for SLA additive manufacturing materials." *Polymers* 13.7 (2021): 1147.

[96] Brinker, C. Jeffrey. "Dip coating." *Chemical Solution Deposition of Functional Oxide Thin Films*. Vienna: Springer Vienna, 2013. 233-261.

[97] Al-Mamun, M. R., et al. "Photocatalytic activity improvement and application of UV-TiO2 photocatalysis in textile wastewater treatment: A review." *Journal of Environmental Chemical Engineering* 7.5 (2019): 103248.

[98] Nur, Alam SM, et al. "A review on the development of elemental and codoped TiO2 photocatalysts for enhanced dye degradation under UV–vis irradiation." *Journal of Water Process Engineering*47 (2022): 102728.

[99] Varnagiris, Sarunas, et al. "Floating TiO2 photocatalyst for efficient inactivation of E. coli and decomposition of methylene blue solution." *Science of the Total Environment* 720 (2020): 137600.

[100] Puddu, Valeria, et al. "TiO2 photocatalyst for indoor air remediation: Influence of crystallinity, crystal phase, and UV radiation intensity on trichloroethylene degradation." *Applied Catalysis B: Environmental* 94.3-4 (2010): 211-218.

[101] Meng, Xiangchao, et al. "Solar photocatalysis for environmental remediation." *Handbook of smart photocatalytic materials*. Elsevier, 2020. 183-195.

[102] Zhang, Ying, et al. "Photodegradation pathway of rhodamine B with novel Au nanorods@ ZnO microspheres driven by visible light irradiation." *Journal of Materials Science* 53 (2018): 3149-3162.

[103] Chen, Feng, Jincai Zhao, and Hisao Hidaka. "Highly selective deethylation of rhodamine B: Adsorption and photooxidation pathways of the dye on the TiO 2/SiO 2 composite photocatalyst." *International Journal of Photoenergy* 5 (2003): 209-217.

[104] Huang, Ni, et al. "One-step pyrolytic synthesis of ZnO nanorods with enhanced photocatalytic activity and high photostability under visible light and UV light irradiation." *Journal of Alloys and Compounds* 648 (2015): 919-929.

[105] He, Zhong, et al. "Photocatalytic degradation of rhodamine B by Bi2WO6 with electron accepting agent under microwave irradiation: mechanism and pathway." *Journal of Hazardous Materials* 162.2-3 (2009): 1477-1486.

[106] Akir, Sana, et al. "Eco-friendly synthesis of ZnO nanoparticles with different morphologies and their visible light photocatalytic performance for the degradation of Rhodamine B." *Ceramics International* 42.8 (2016): 10259-10265.

[107] Rochkind, Malka, Sagi Pasternak, and Yaron Paz. "Using dyes for evaluating photocatalytic properties: a critical review." *Molecules* 20.1 (2014): 88-110.

[108] Ferreira, Sofia Henriques, et al. "High UV and sunlight photocatalytic performance of porous ZnO nanostructures synthesized by a facile and fast microwave hydrothermal method." *Materials* 14.9 (2021): 2385.

[109] Ren, Wenjie, et al. "Low temperature preparation and visible light photocatalytic activity of mesoporous carbon-doped crystalline TiO2." *Applied Catalysis B: Environmental* 69.3-4 (2007): 138-144.

[110] Wang, Ji-Chao, et al. "Natural sunlight driven highly efficient photocatalysis for simultaneous degradation of rhodamine B and methyl orange using I/C codoped TiO2 photocatalyst." *Journal of hazardous materials* 360 (2018): 356-363.

[111] Thostenson, E. T., and T-W. Chou. "Microwave processing: fundamentals and applications." *Composites Part A: Applied Science and Manufacturing* 30.9 (1999): 1055-1071.

[112] Pimentel, Ana, et al. "Photocatalytic activity of TiO2 nanostructured arrays prepared by microwave-assisted solvothermal method." *Semiconductor Photocatalysis—Materials, Mechanisms and Applications* (2016).

[113] Veggi, Priscilla C., Julian Martinez, and M. Angela A. Meireles. "Fundamentals of microwave extraction." *Microwave-assisted extraction for bioactive compounds: theory and practice*. Boston, MA: Springer US, 2012. 15-52.

[114] Karpovich, N. F., M. A. Pugachevskii, and D. S. Shtarev. "Influence of synthesis conditions on the shape and size characteristics of TiO 2 nanocrystals." *Nanotechnologies in Russia* 8 (2013): 751-755

[115] Wu, ZhongBiao, et al. "Photocatalytic oxidation of gaseous benzene over nanosized TiO2 prepared by solvothermal method." *Chinese Science Bulletin* 52.22 (2007): 3061-3067.

[116] Zhou, Yi, et al. "Effects of non-polar solvent on the morphology and property of three-dimensional hierarchical TiO 2 nanostructures by one-step solvothermal route." *Journal of nanoparticle research* 16 (2014): 1-9.

[117] Wu, Yu-Chun, and Yu-Chuen Tai. "Effects of alcohol solvents on anatase TiO 2 nanocrystals prepared by microwave-assisted solvothermal method." *Journal of nanoparticle research* 15 (2013): 1-11.

[118] Freire, Tomás, et al. "Enhanced solar photocatalysis of TiO2 nanoparticles and nanostructured thin films grown on paper." *Nano Express* 2.4 (2021): 040002.

[119] Guo, Yanna, et al. "TiO 2 mesocrystals built of nanocrystals with exposed {001} facets: Facile synthesis and superior photocatalytic ability." *Journal of Materials Chemistry A* 2.46 (2014): 19589-19593.

[120] Pan, Feng, et al. "Synthesis of {100} facet dominant anatase TiO2 nanobelts and the origin of facet-dependent photoreactivity." *Chemistry–A European Journal* 20.46 (2014): 15095-15101.

[121] Xu, Hua, et al. "High-active anatase TiO2 nanosheets exposed with 95%{100} facets toward efficient H2 evolution and CO2 photoreduction." *ACS applied materials & interfaces* 5.4 (2013): 1348-1354.

[122] Nakata, Kazuya, and Akira Fujishima. "TiO2 photocatalysis: Design and applications." *Journal of photochemistry and photobiology C: Photochemistry Reviews* 13.3 (2012): 169-189.

[123] Peng, Tianyou, et al. "Synthesis of titanium dioxide nanoparticles with mesoporous anatase wall and high photocatalytic activity." *The journal of physical chemistry B* 109.11 (2005): 4947-4952.

[124] Mohamed, Reda M., et al. "A comparative study on mesoporous and commercial TiO2 photocatalysts for photodegradation of organic pollutants." *Journal of Photochemistry and Photobiology A: Chemistry* 367 (2018): 66-73.

[125] Sarah, M. S. P., et al. "Crack-free TiO2 thin film via sol-gel dip coating method: investigation on molarity effect." *IOP Conference Series: Materials Science and Engineering*. Vol. 340. No. 1. IOP Publishing, 2018.

[126] Carrington, Nathan A., Li Yong, and Zi-Ling Xue. "Electrochemical deposition of sol–gel films for enhanced chromium (VI) determination in aqueous solutions." *Analytica chimica acta* 572.1 (2006): 17-24.

[127] Hemissi, M., H. Amardjia-Adnani, and J. C. Plenet. "Titanium oxide thin layers deposed by dip-coating method: Their optical and structural properties." *Current Applied Physics* 9.4 (2009): 717-721.

[128] Ramos, Francisco, et al. "IST-LASAGNE: Towards all-optical label swapping employing optical logic gates and optical flip-flops." *Journal of Lightwave Technology* 23.10 (2005): 2993.